Supplement of Nat. Hazards Earth Syst. Sci., 26, 5167–5184, 2026
https://doi.org/10.5194/nhess-26-5167-2026-supplement
© Author(s) 2026. CC BY 4.0 License.



Natural Hazards and Earth System Sciences
Open Access
EGU

Supplement of

Distinguishing run-up height from pressure distribution during avalanche impact on narrow obstacles: mechanisms and semi-empirical prediction from three-dimensional simulations

Michael J. Kohler et al.

Correspondence to: Michael J. Kohler (michael.kohler@slf.ch)

The copyright of individual parts of the supplement might differ from the article licence.

Contents

S1 Definitions and calculation procedures **2**
S1.1 Derivation of the plastic compressibility parameter 2
S1.2 Volume-averaging procedure 2

S2 Sensitivity analysis **4**

S3 Visuals of flow morphology **8**

S4 Time histories **15**

S5 Peak values to steady-state values **28**

S6 Rheological decomposition **29**

S7 Impact pressure profiles **36**

S8 Semi-empirical modeling **43**
S8.1 Performance metrics 43
S8.2 Run-up height 44
S8.3 Pressure height 44

S9 Velocity sweep of the calculation examples **47**
S9.1 Original scenario: dry, loose impact 47
S9.2 Modified scenario: dense impact 47

S1 Definitions and calculation procedures

S1.1 Derivation of the plastic compressibility parameter

The plastic compressibility parameter $\chi(p_c = 25)$ serves as a factor (in %) that quantifies how much the material densifies under compression at an arbitrarily chosen reference pre-consolidation pressure of 25 kPa (following our previous publication Kohler et al., 2026). We derive it by rearranging Eq. (4) in the body of the article

$$J_P(p_c) = \exp\left(-\sinh^{-1}(p_c/K)/\xi\right), \tag{S1}$$

where $J_P = \exp \varepsilon_V^P$. Using $\chi = 1/J_P = \rho/\rho_0$ and evaluating at $p_c = 25\,\mathrm{kPa}$ yields

$$\chi(p_c = 25) = J_P(p_{c,0}) \,/\, J_P(25\,\mathrm{kPa}), \tag{S2}$$

where the numerator corresponds to the initial kinematic configuration under the initial pre-consolidation pressure $p_{c,0}$. We stress that the reference pressure of 25 kPa is a normalization constant, and its choice affects only how compressibility is labeled, not the results. For a given hardening parameter, Equation (S1) and Equation (S2) map monotonically onto the density-increase factor. A different reference pressure would rescale the density-increase factor without changing its one-to-one correspondence with the hardening parameter, and therefore without changing any result or fit.

S1.2 Volume-averaging procedure

An MP property x is volume-averaged within a domain D by weighting the individual property of each MP i with its Jacobian J_i through

$$\langle x \rangle_D = \frac{\sum_{i=1}^{n} x_i J_i}{\sum_{i=1}^{n} J_i}, \tag{S3}$$

where n is the number of MPs in the averaging domain. Here we use the angle brackets to denote volume-averaged quantities. For impact pressure, which we define as the flow-wise component σ_{xx} of the Cauchy stress tensor, this relation simplifies to

$$\langle \sigma_{xx} \rangle_D = \frac{\sum_{i=1}^{n} \tau_{xx,i}}{\sum_{i=1}^{n} J_i}, \tag{S4}$$

where we utilized the identity $\boldsymbol{\sigma} = \boldsymbol{\tau}/J$.

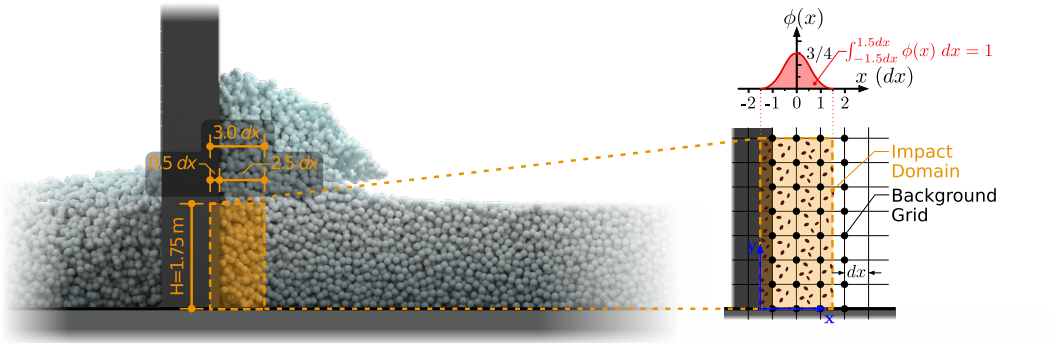
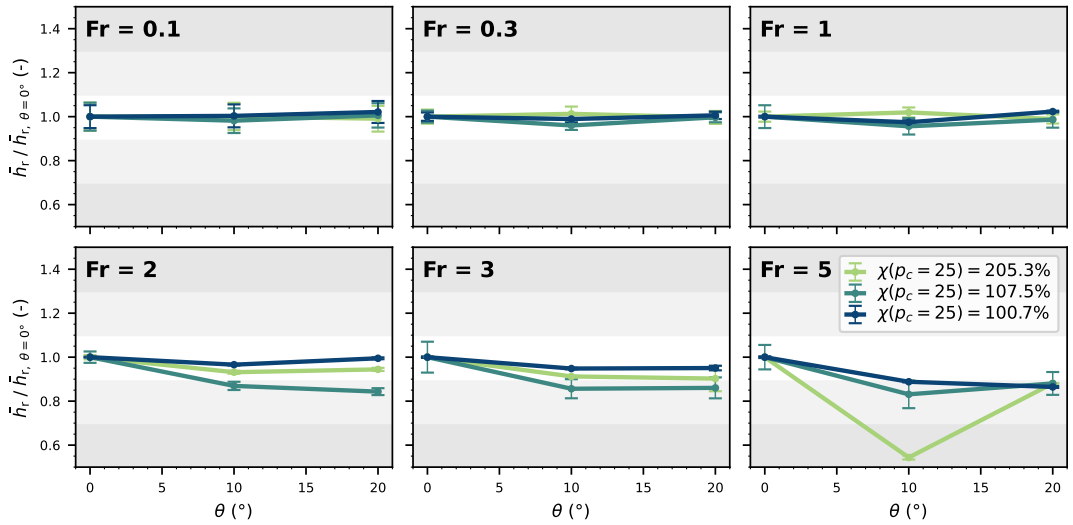


Figure S1. Illustration of the impact domain, showing the quadratic B-spline interpolation functions and their extent at an exemplary MP in the x-direction (taken from Kohler et al., 2026)

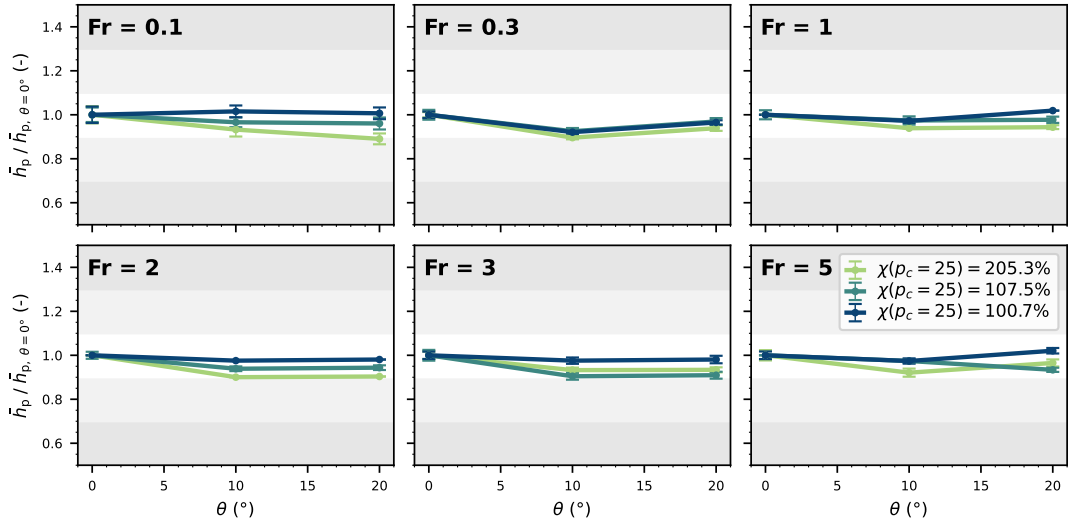
To calculate a depth-averaged impact pressure, we perform this procedure in the *impact domain*. This fixed volume extends almost over the entire width of the obstacle ($1.5\,\mathrm{m}$), and its height matches the initial flow height of $1.75\,\mathrm{m}$. The upstream extent ranges from $x = -0.5dx$ to $x = 2.5dx$ and was selected to (i) cover the range of the quadratic B-spline interpolation functions rising to $3dx$ as visualized in Figure S1 and (ii) capture the particles which slightly penetrate the obstacle, which is commonly observed in MPM.

For a volume-averaged compaction measure, it proved more robust to track the total mass of all particles within the impact region, excluding the portion that extends into the obstacle. We then divide this mass by the volume of the region and compare it to the original (reference) density.

S2 Sensitivity analysis

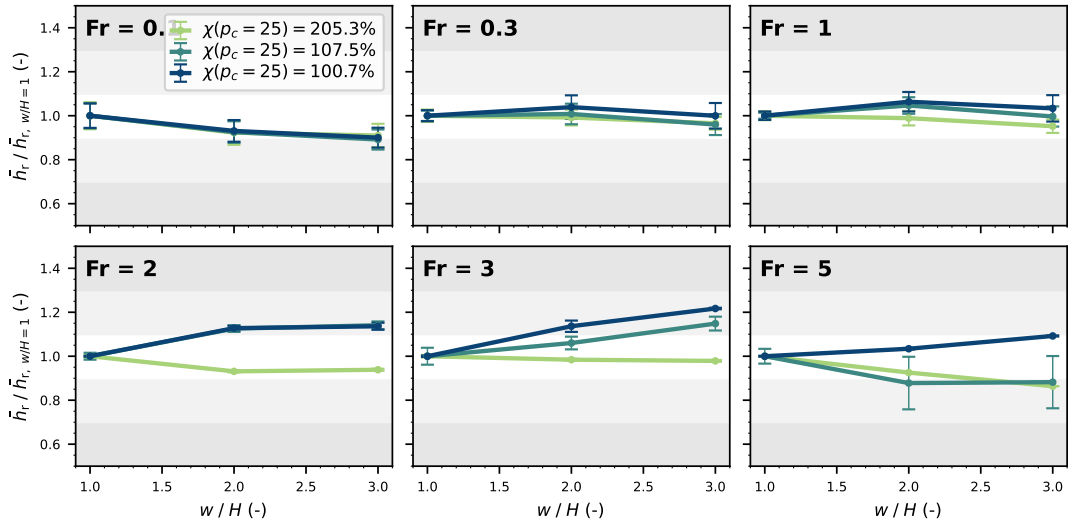


(a) Run-up height

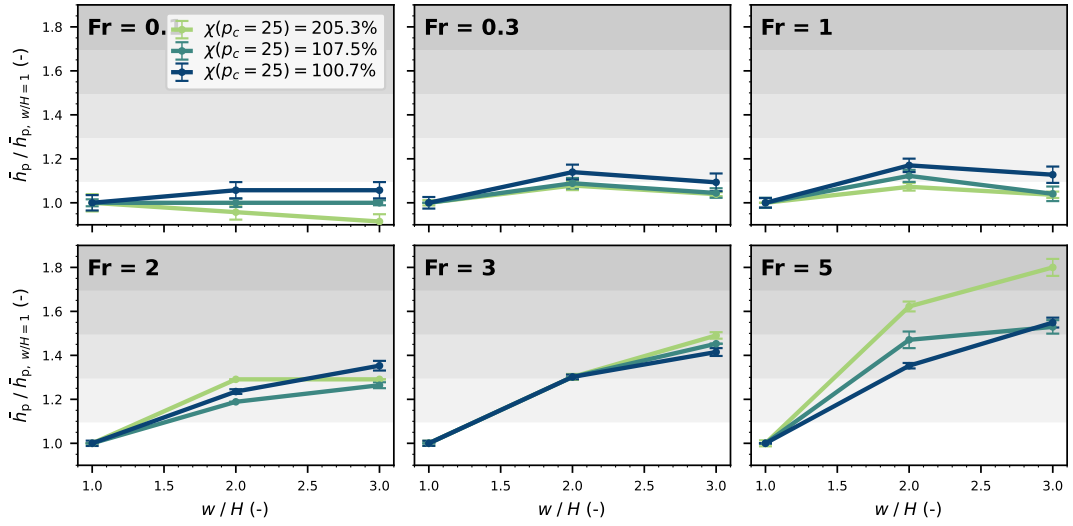


(b) Pressure height

Figure S2. Influence of slope angle

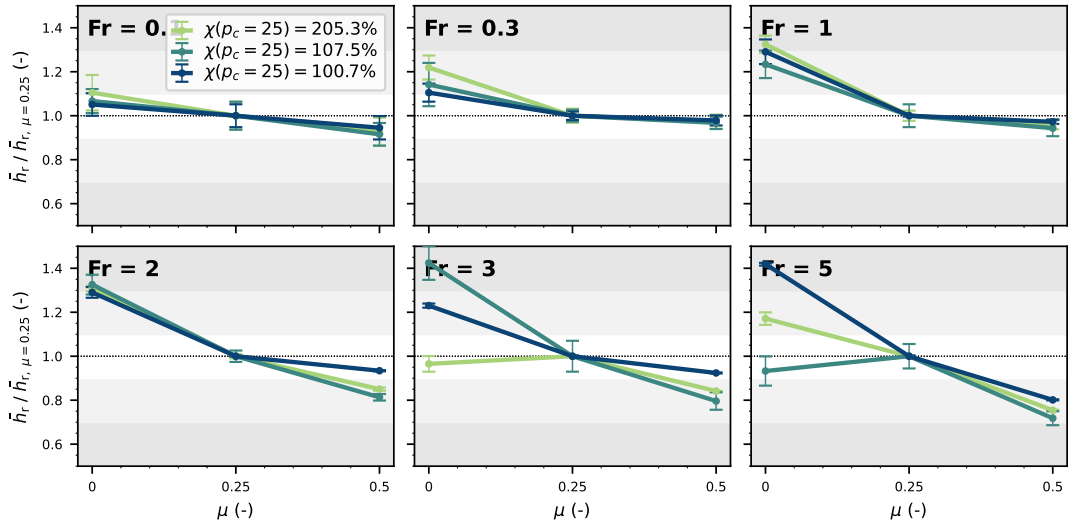


(a) Run-up height

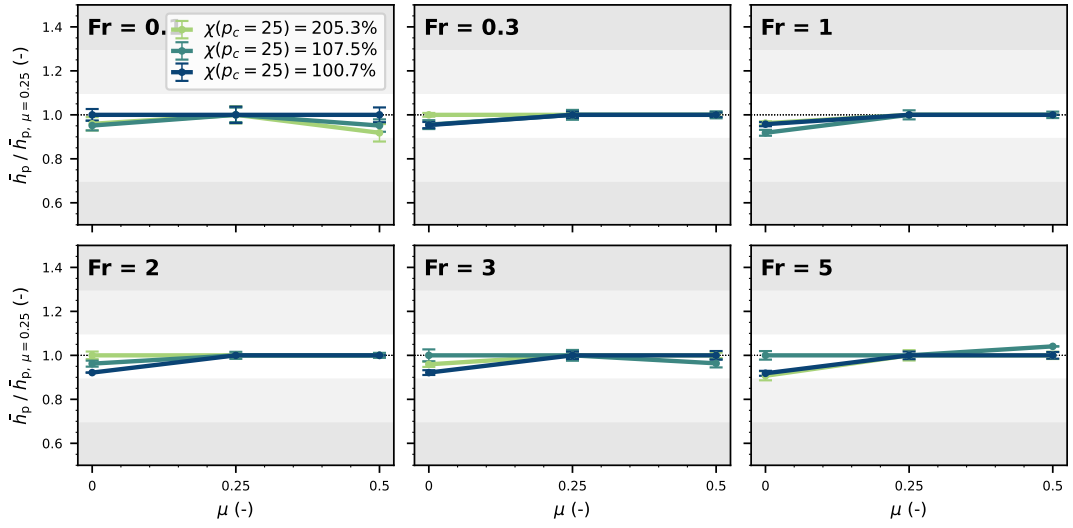


(b) Pressure height

Figure S3. Influence of obstacle width



(a) Run-up height



(b) Pressure height

Figure S4. Influence of obstacle friction

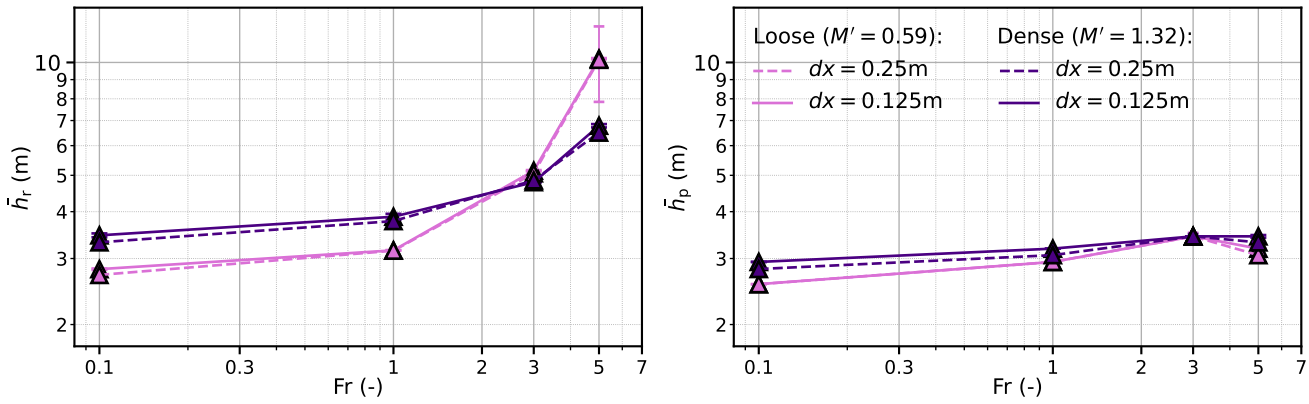
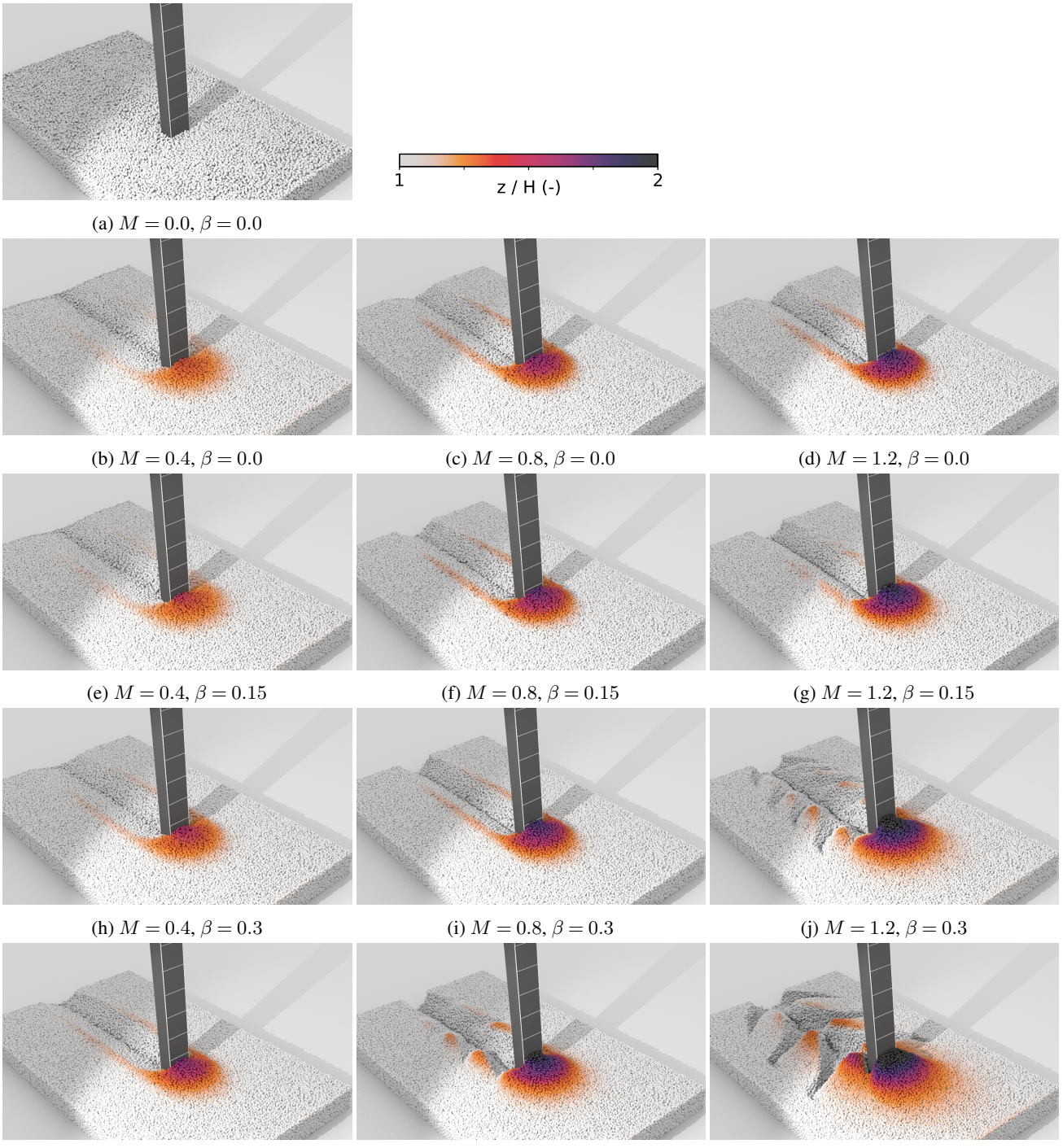


Figure S5. Mesh study on run-up and pressure height for dry, loose and dense snow avalanche rheology for various Fr

S3 Visuals of flow morphology

Cf. subsequent pages.



(a) $M = 0.0$, $\beta = 0.0$

(b) $M = 0.4$, $\beta = 0.0$

(c) $M = 0.8$, $\beta = 0.0$

(d) $M = 1.2$, $\beta = 0.0$

(e) $M = 0.4$, $\beta = 0.15$

(f) $M = 0.8$, $\beta = 0.15$

(g) $M = 1.2$, $\beta = 0.15$

(h) $M = 0.4$, $\beta = 0.3$

(i) $M = 0.8$, $\beta = 0.3$

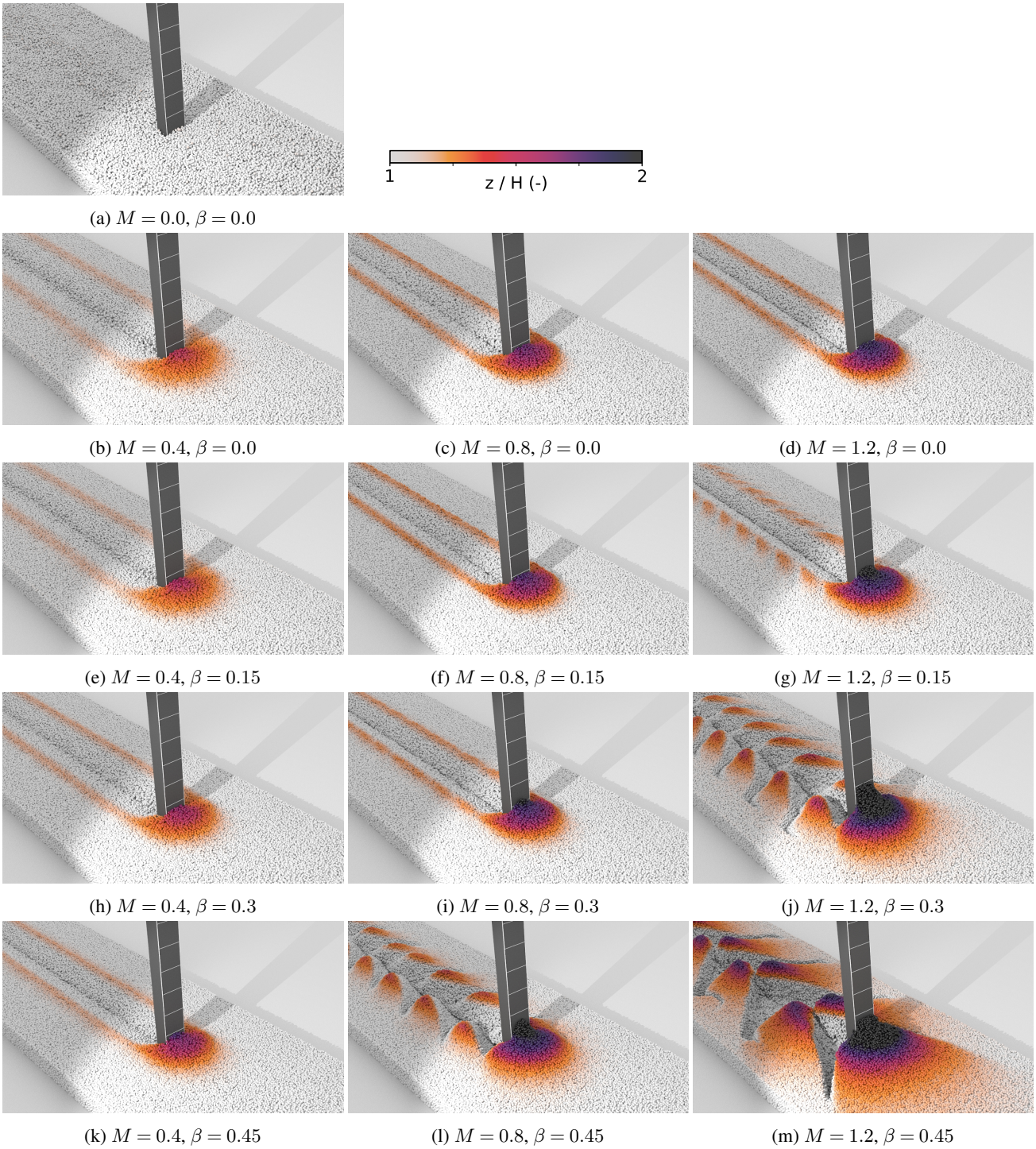
(j) $M = 1.2$, $\beta = 0.3$

(k) $M = 0.4$, $\beta = 0.45$

(l) $M = 0.8$, $\beta = 0.45$

(m) $M = 1.2$, $\beta = 0.45$

Figure S6. Fr $= 0.1$ and $\xi = 0.5$



(a) $M = 0.0$, $\beta = 0.0$

(b) $M = 0.4$, $\beta = 0.0$

(c) $M = 0.8$, $\beta = 0.0$

(d) $M = 1.2$, $\beta = 0.0$

(e) $M = 0.4$, $\beta = 0.15$

(f) $M = 0.8$, $\beta = 0.15$

(g) $M = 1.2$, $\beta = 0.15$

(h) $M = 0.4$, $\beta = 0.3$

(i) $M = 0.8$, $\beta = 0.3$

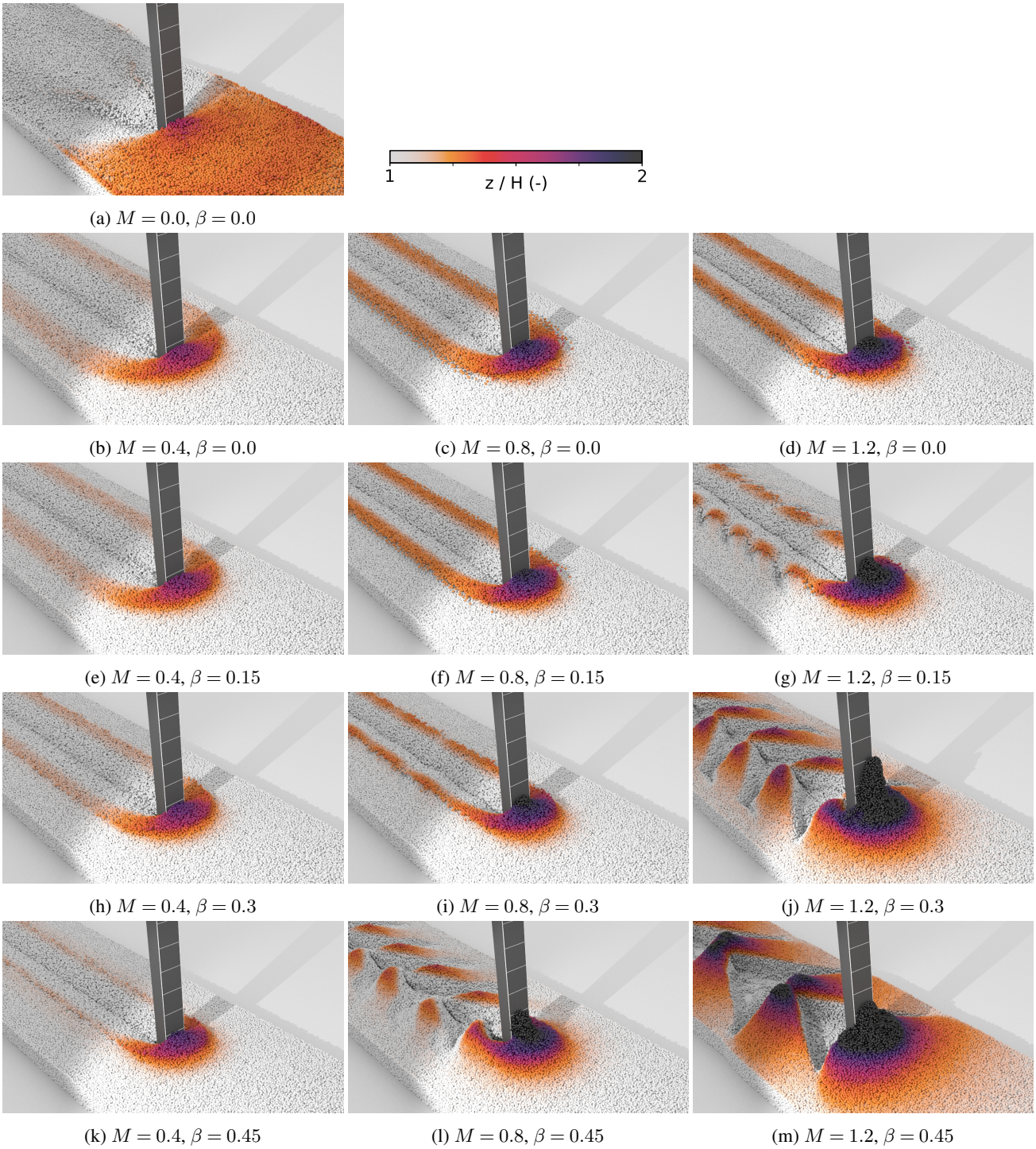
(j) $M = 1.2$, $\beta = 0.3$

(k) $M = 0.4$, $\beta = 0.45$

(l) $M = 0.8$, $\beta = 0.45$

(m) $M = 1.2$, $\beta = 0.45$

Figure S7. $\mathrm{Fr} = 0.3$ and $\xi = 0.5$



(a) $M = 0.0$, $\beta = 0.0$

(b) $M = 0.4$, $\beta = 0.0$

(c) $M = 0.8$, $\beta = 0.0$

(d) $M = 1.2$, $\beta = 0.0$

(e) $M = 0.4$, $\beta = 0.15$

(f) $M = 0.8$, $\beta = 0.15$

(g) $M = 1.2$, $\beta = 0.15$

(h) $M = 0.4$, $\beta = 0.3$

(i) $M = 0.8$, $\beta = 0.3$

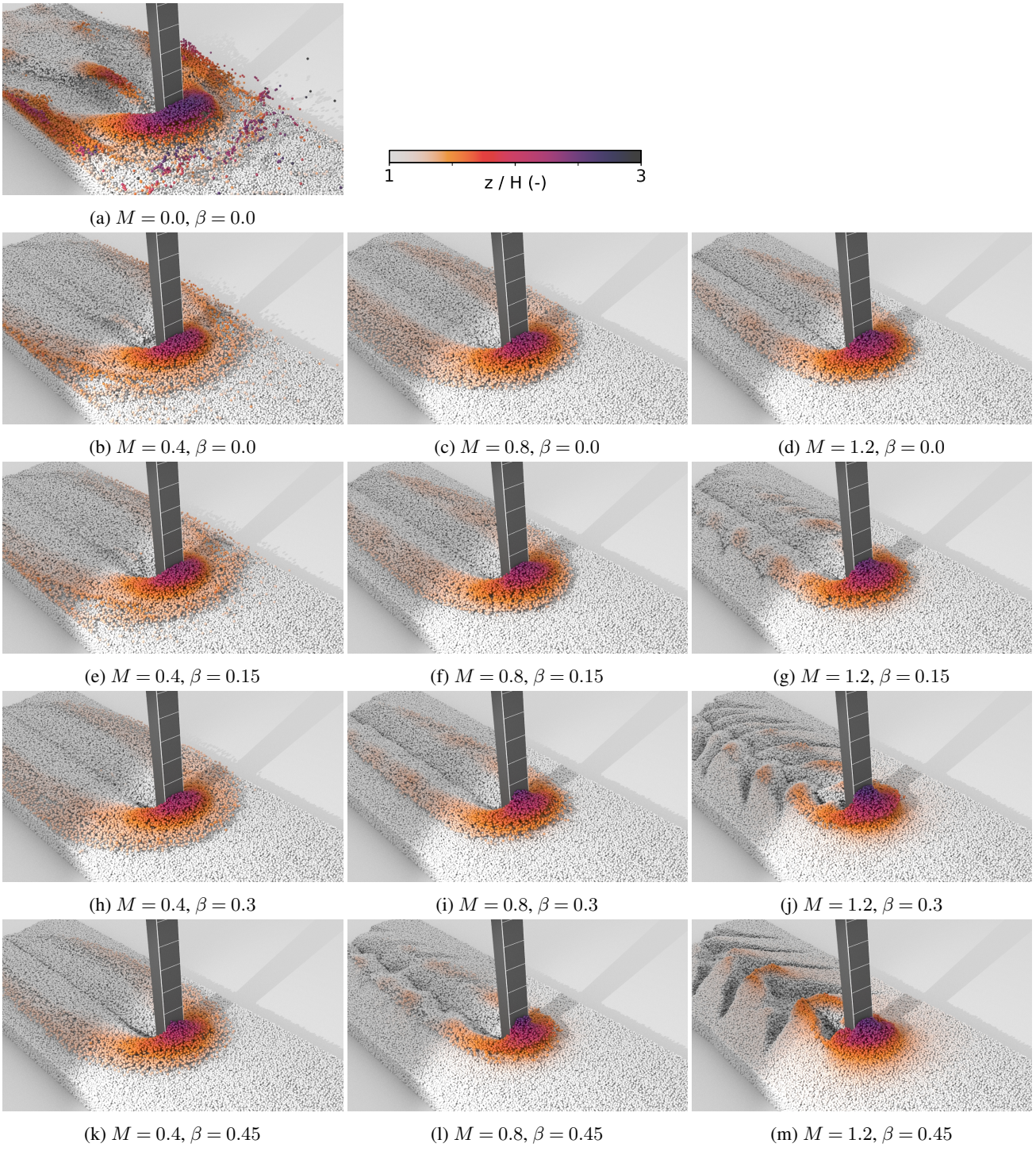
(j) $M = 1.2$, $\beta = 0.3$

(k) $M = 0.4$, $\beta = 0.45$

(l) $M = 0.8$, $\beta = 0.45$

(m) $M = 1.2$, $\beta = 0.45$

Figure S8. Fr $= 1$ and $\xi = 0.5$



(a) $M = 0.0$, $\beta = 0.0$

(b) $M = 0.4$, $\beta = 0.0$

(c) $M = 0.8$, $\beta = 0.0$

(d) $M = 1.2$, $\beta = 0.0$

(e) $M = 0.4$, $\beta = 0.15$

(f) $M = 0.8$, $\beta = 0.15$

(g) $M = 1.2$, $\beta = 0.15$

(h) $M = 0.4$, $\beta = 0.3$

(i) $M = 0.8$, $\beta = 0.3$

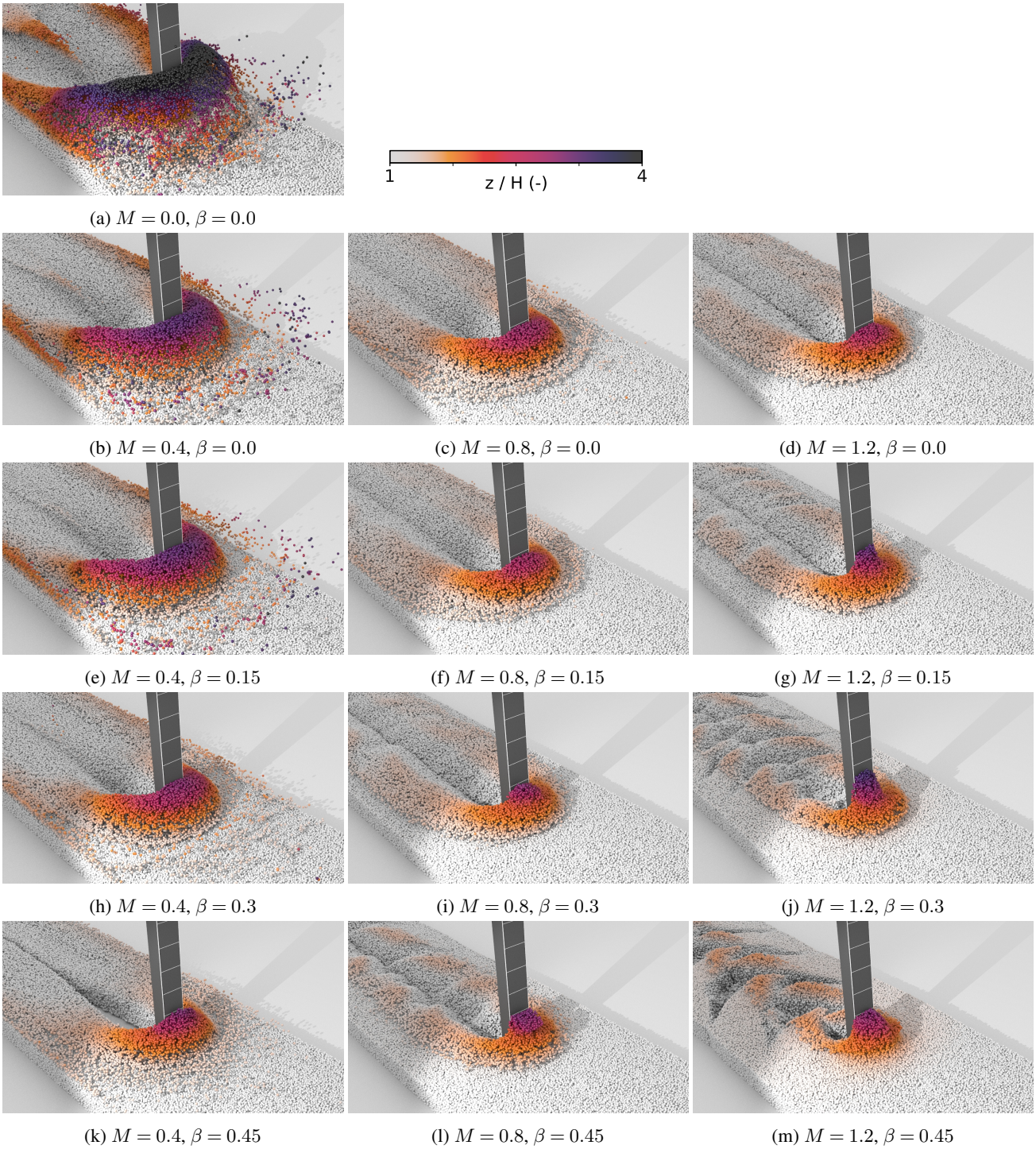
(j) $M = 1.2$, $\beta = 0.3$

(k) $M = 0.4$, $\beta = 0.45$

(l) $M = 0.8$, $\beta = 0.45$

(m) $M = 1.2$, $\beta = 0.45$

Figure S9. Fr $= 2$ and $\xi = 0.5$



(a) $M = 0.0$, $\beta = 0.0$

(b) $M = 0.4$, $\beta = 0.0$

(c) $M = 0.8$, $\beta = 0.0$

(d) $M = 1.2$, $\beta = 0.0$

(e) $M = 0.4$, $\beta = 0.15$

(f) $M = 0.8$, $\beta = 0.15$

(g) $M = 1.2$, $\beta = 0.15$

(h) $M = 0.4$, $\beta = 0.3$

(i) $M = 0.8$, $\beta = 0.3$

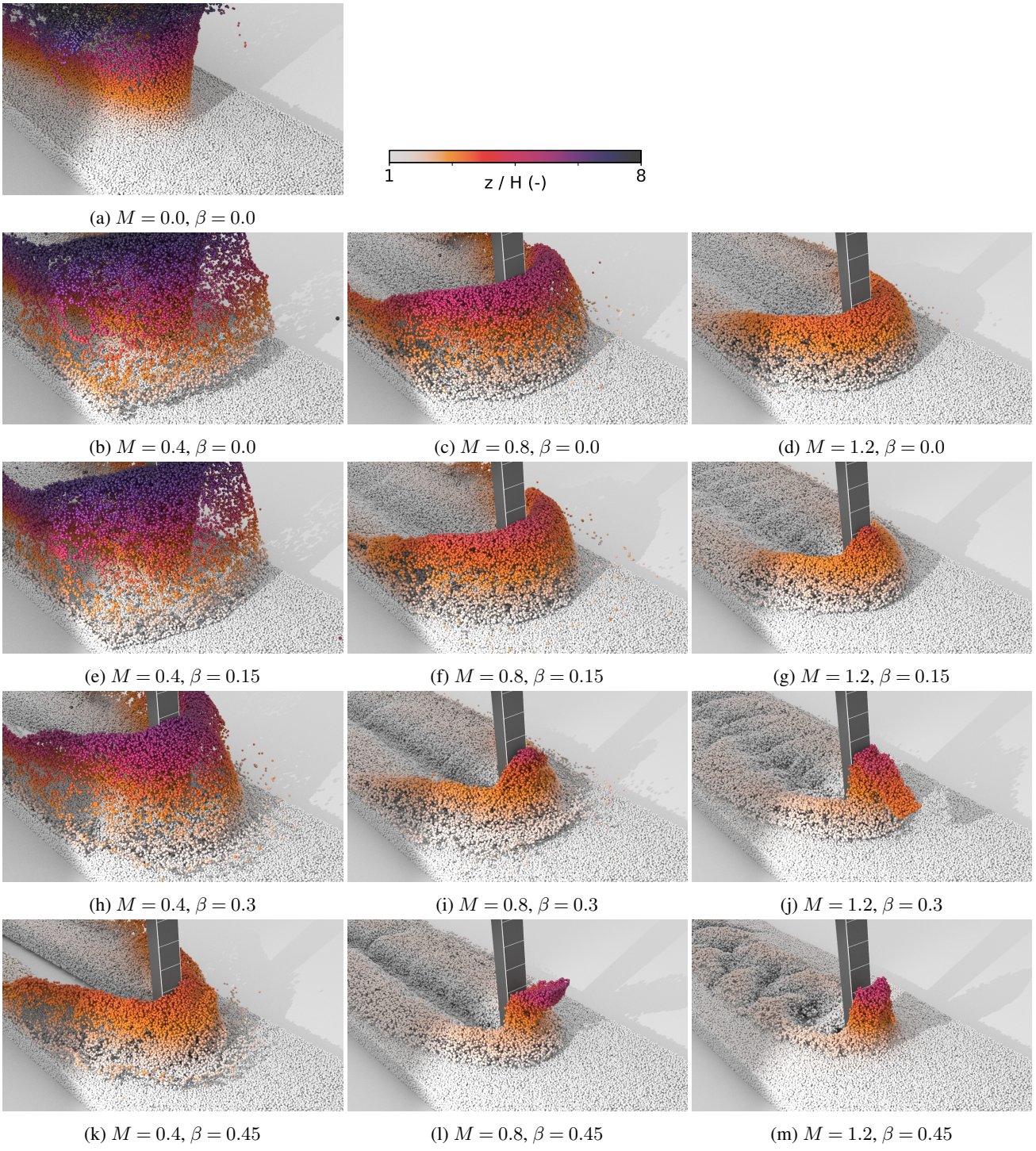
(j) $M = 1.2$, $\beta = 0.3$

(k) $M = 0.4$, $\beta = 0.45$

(l) $M = 0.8$, $\beta = 0.45$

(m) $M = 1.2$, $\beta = 0.45$

Figure S10. Fr $= 3$ and $\xi = 0.5$



(a) $M = 0.0$, $\beta = 0.0$

(b) $M = 0.4$, $\beta = 0.0$

(c) $M = 0.8$, $\beta = 0.0$

(d) $M = 1.2$, $\beta = 0.0$

(e) $M = 0.4$, $\beta = 0.15$

(f) $M = 0.8$, $\beta = 0.15$

(g) $M = 1.2$, $\beta = 0.15$

(h) $M = 0.4$, $\beta = 0.3$

(i) $M = 0.8$, $\beta = 0.3$

(j) $M = 1.2$, $\beta = 0.3$

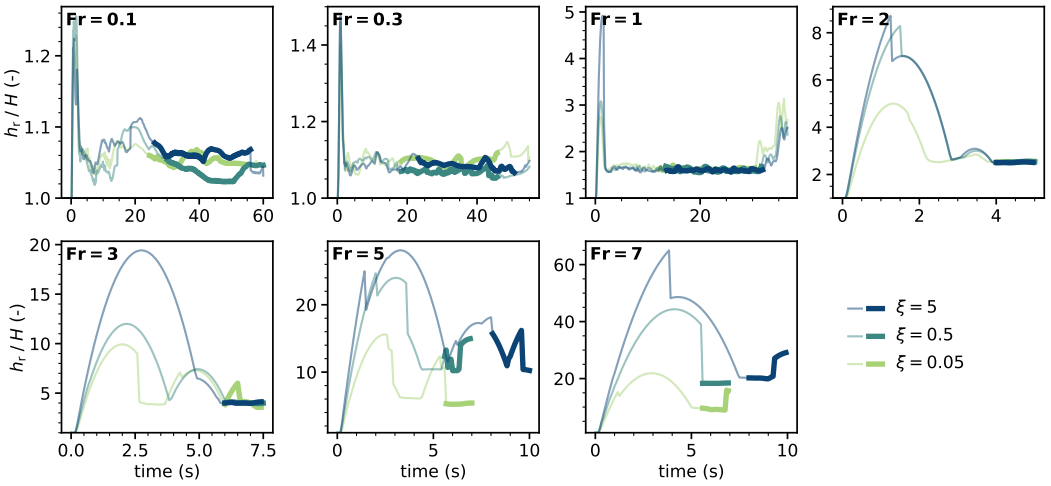
(k) $M = 0.4$, $\beta = 0.45$

(l) $M = 0.8$, $\beta = 0.45$

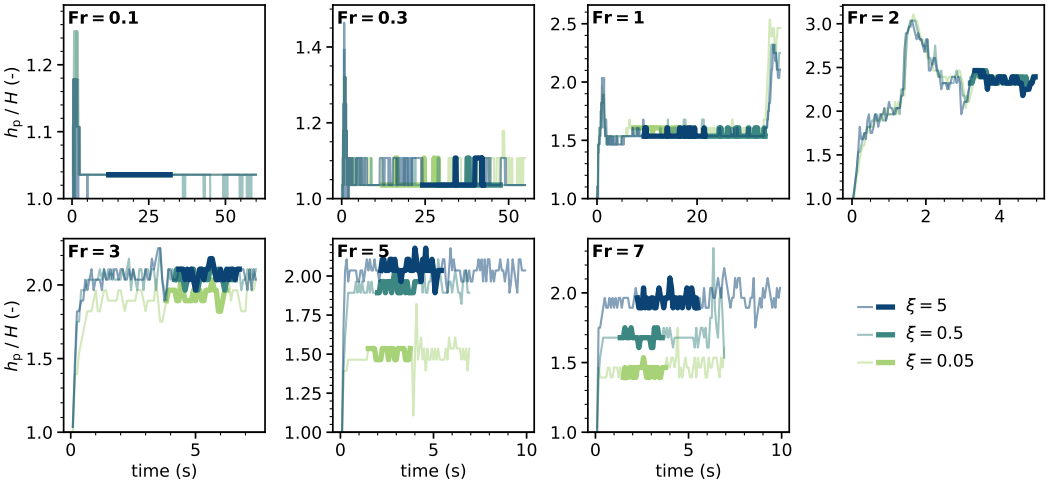
(m) $M = 1.2$, $\beta = 0.45$

Figure S11. Fr $= 5$ and $\xi = 0.5$

S4 Time histories

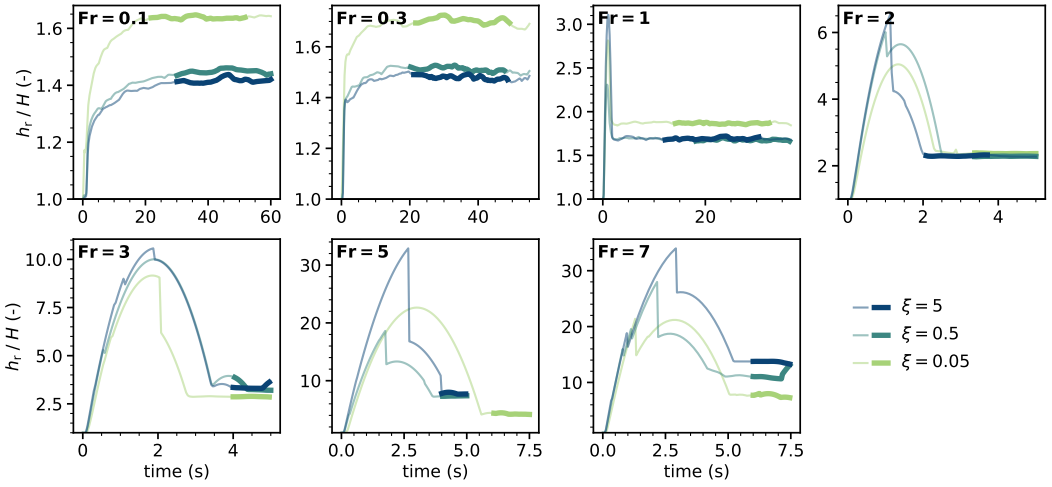


(a) Run-up height

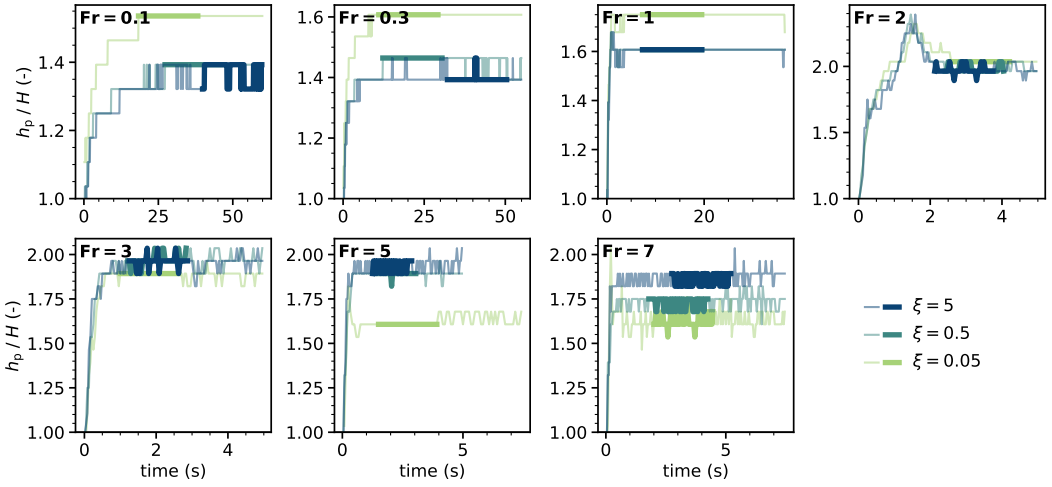


(b) Pressure height

Figure S12. Simulated rheology: $M' = 0$ ($M = 0$; $\beta = 0$)

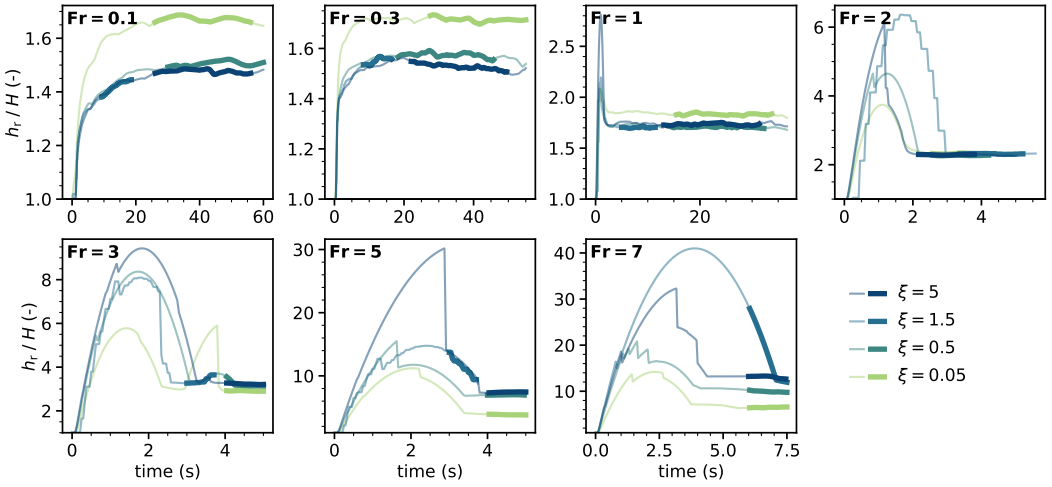


(a) Run-up height

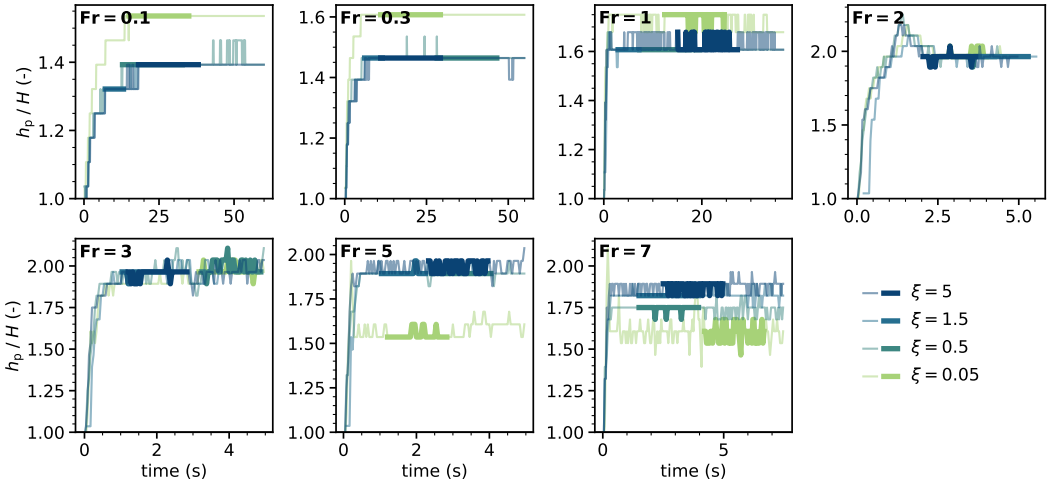


(b) Pressure height

Figure S13. Simulated rheology: $M' = 0.4$ ($M = 0.4$; $\beta = 0$)

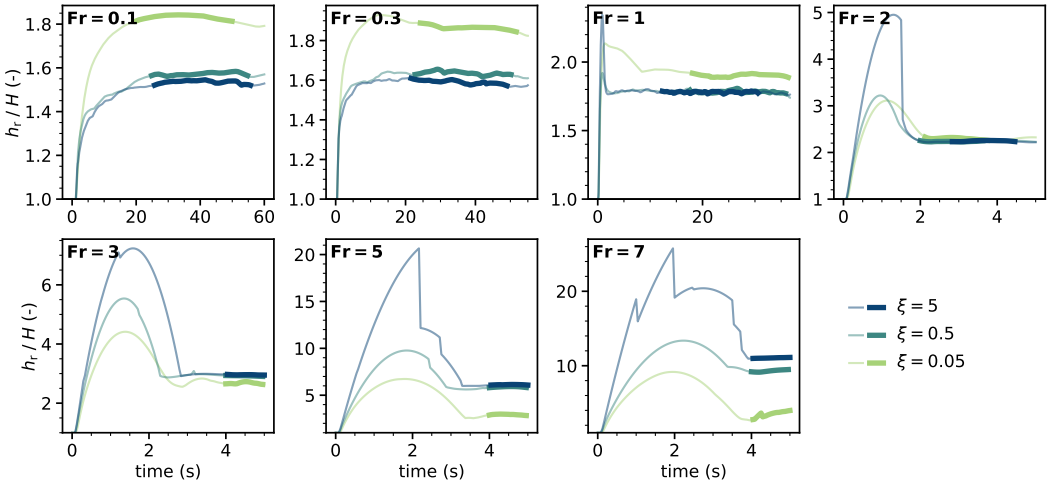


(a) Run-up height

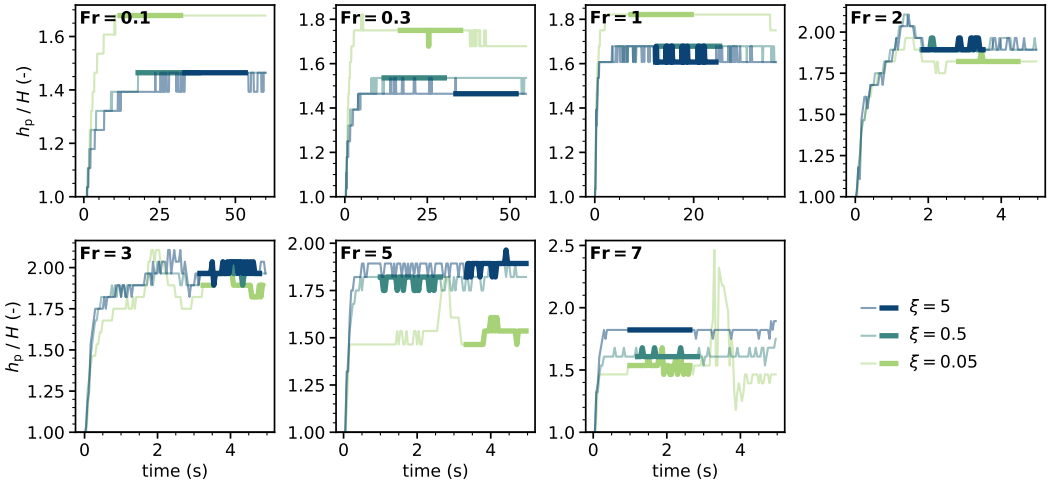


(b) Pressure height

Figure S14. Simulated rheology: $M' = 0.47$ ($M = 0.4$; $\beta = 0.15$)

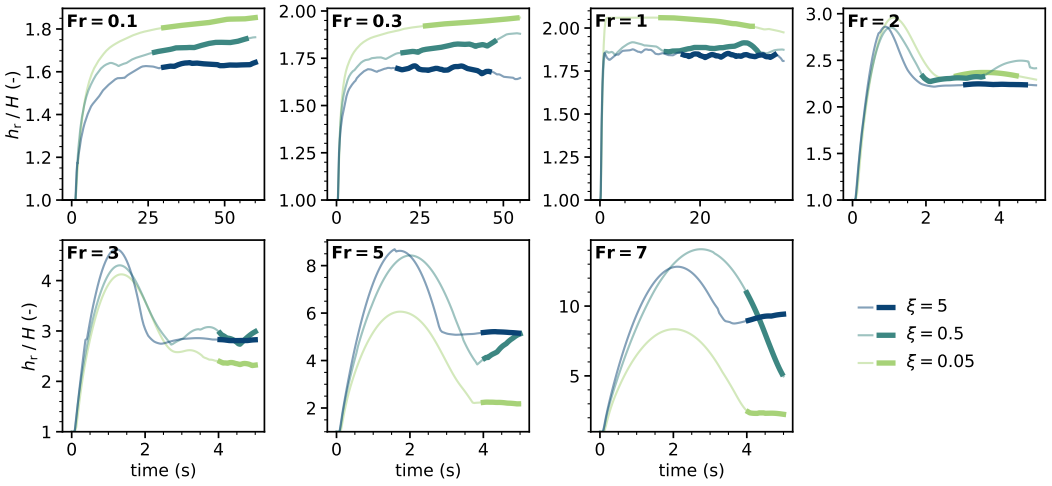


(a) Run-up height

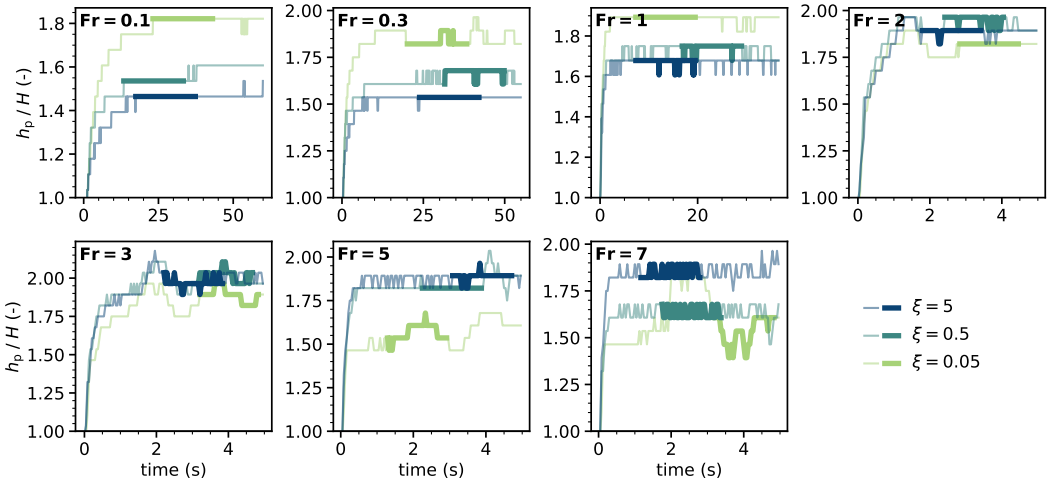


(b) Pressure height

Figure S15. Simulated rheology: $M' = 0.59$ ($M = 0.4$; $\beta = 0.3$)

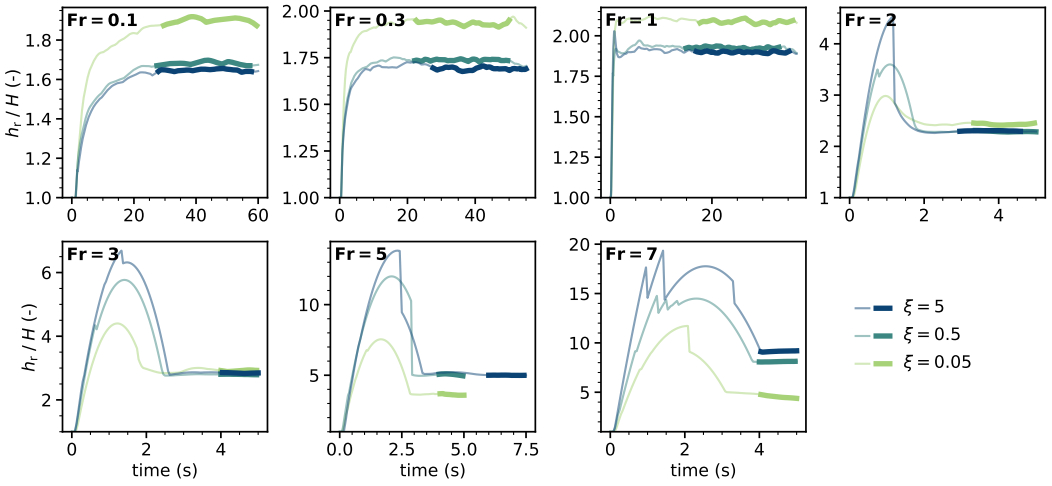


(a) Run-up height

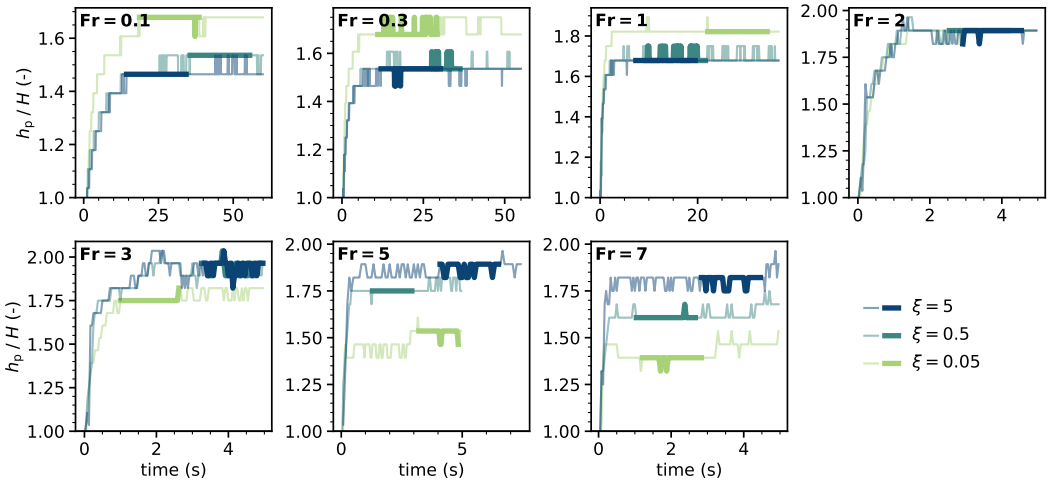


(b) Pressure height

Figure S16. Simulated rheology: $M' = 0.77$ ($M = 0.4$; $\beta = 0.45$)

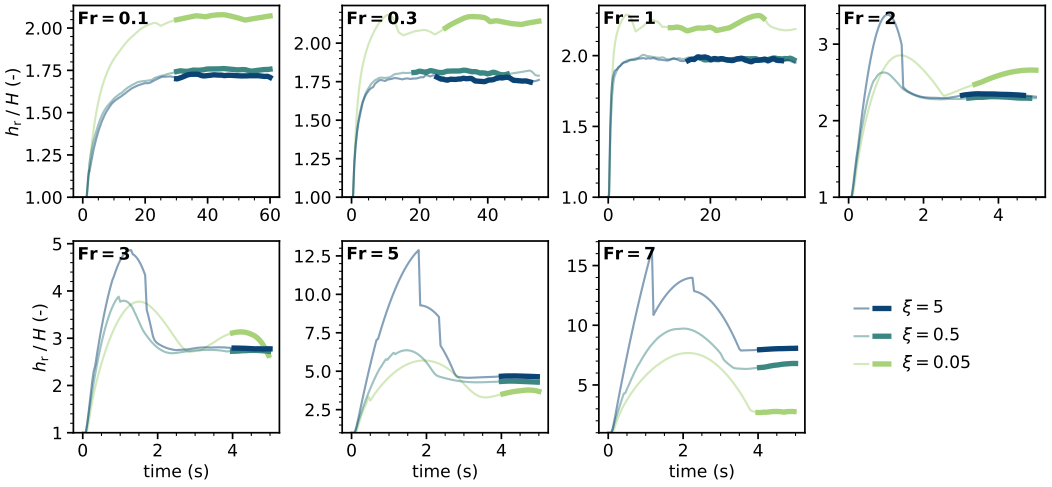


(a) Run-up height

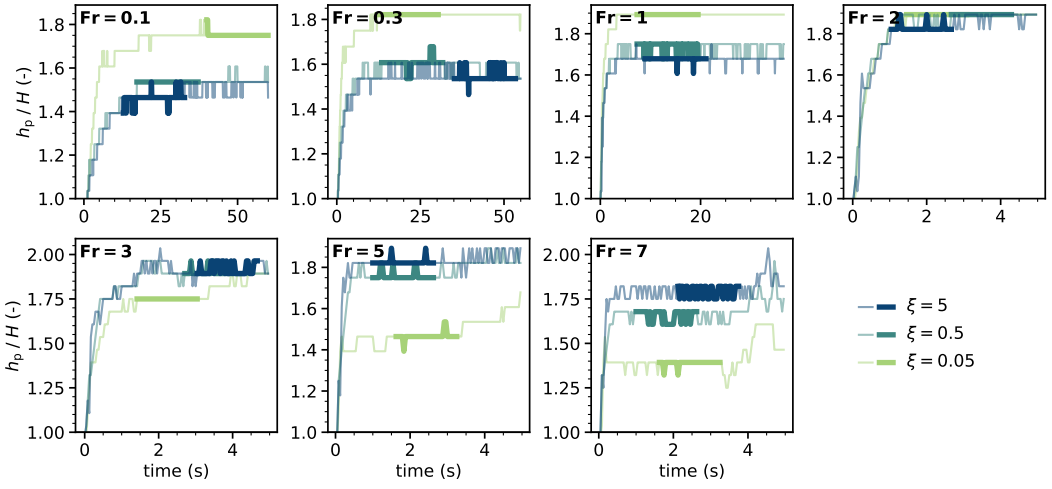


(b) Pressure height

Figure S17. Simulated rheology: $M' = 0.8$ ($M = 0.8$; $\beta = 0$)

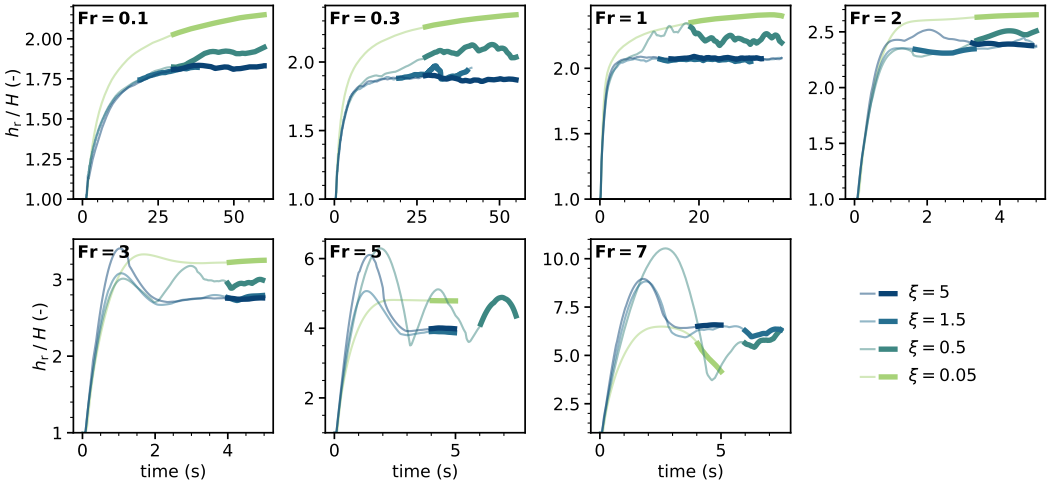


(a) Run-up height

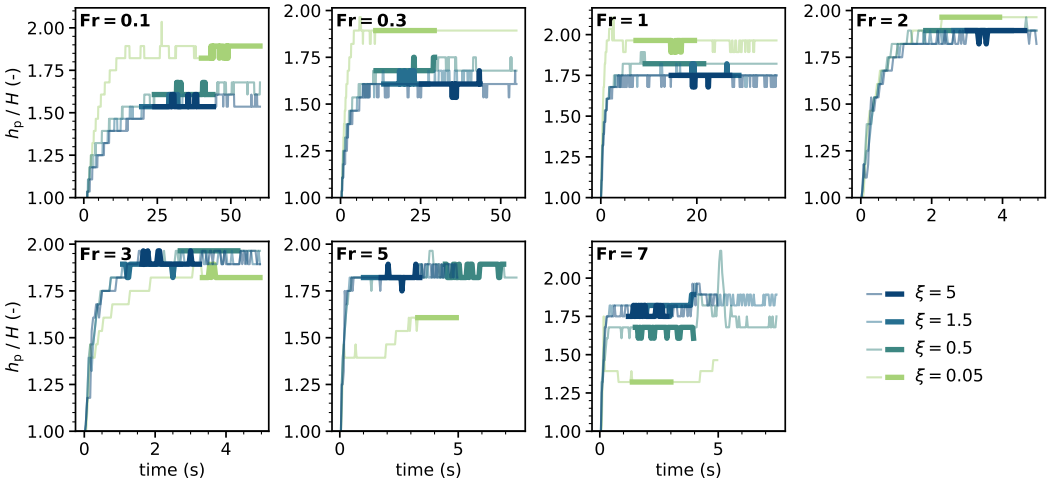


(b) Pressure height

Figure S18. Simulated rheology: $M' = 0.95$ ($M = 0.8$; $\beta = 0.15$)

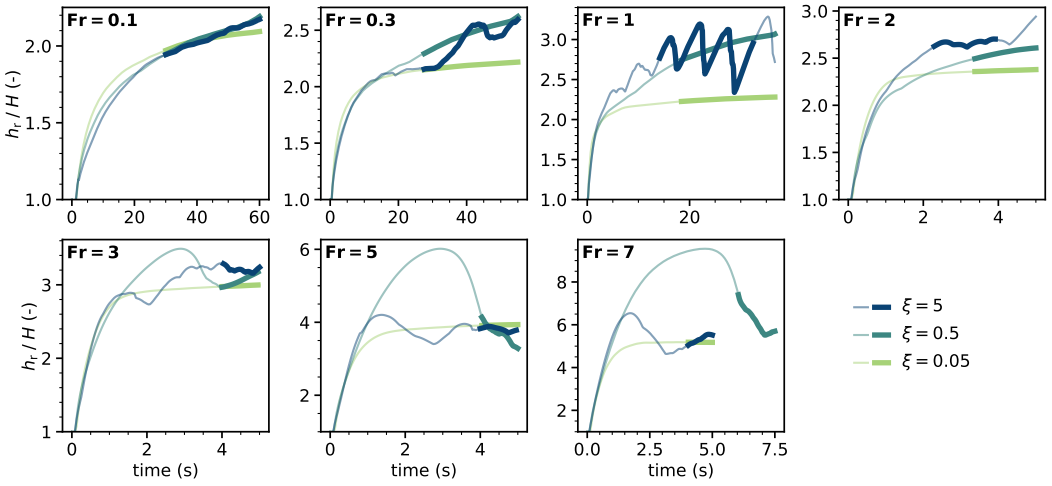


(a) Run-up height

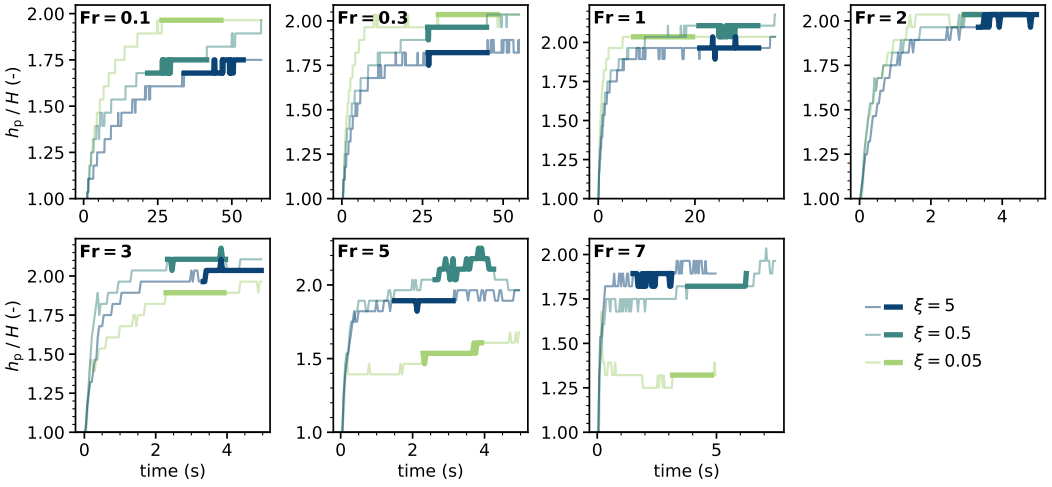


(b) Pressure height

Figure S19. Simulated rheology: $M' = 1.17$ ($M = 0.8$; $\beta = 0.3$)

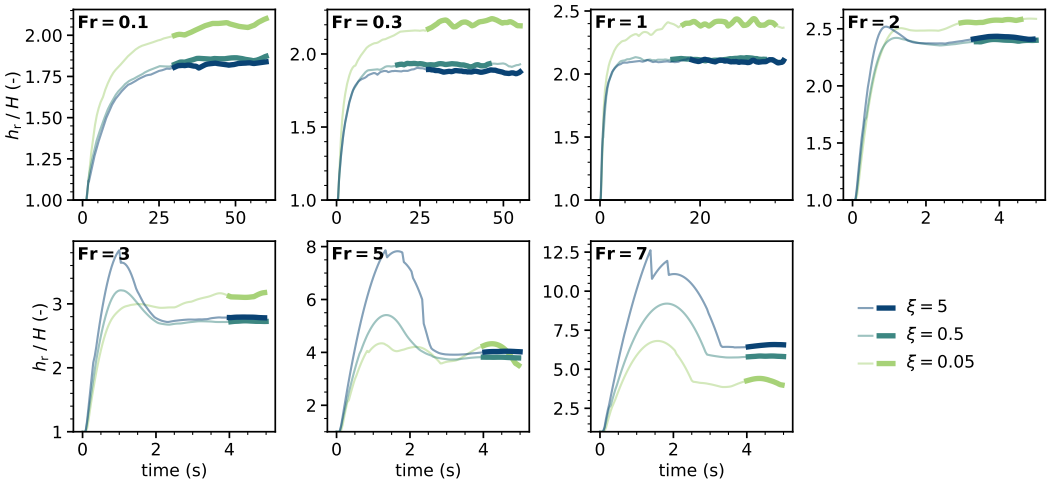


(a) Run-up height

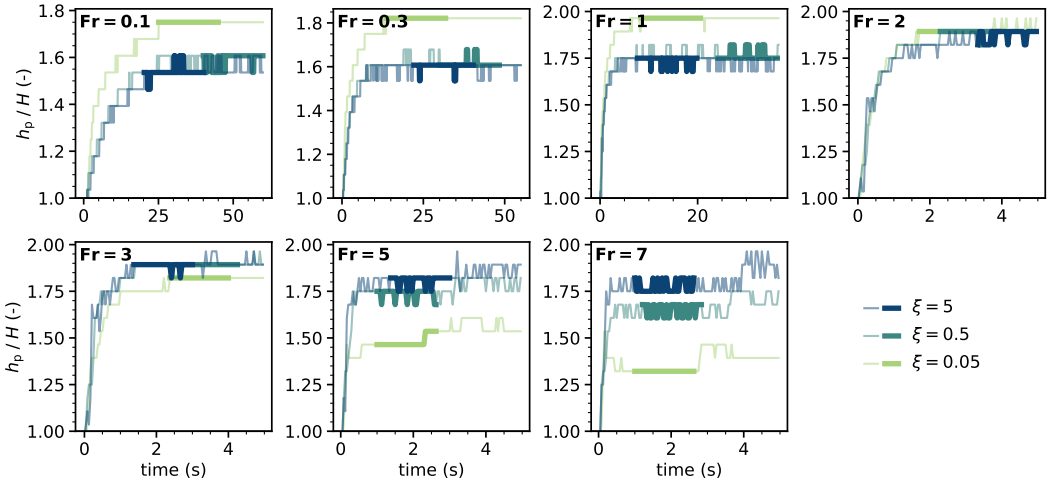


(b) Pressure height

Figure S20. Simulated rheology: $M' = 1.53$ ($M = 0.8$; $\beta = 0.45$)

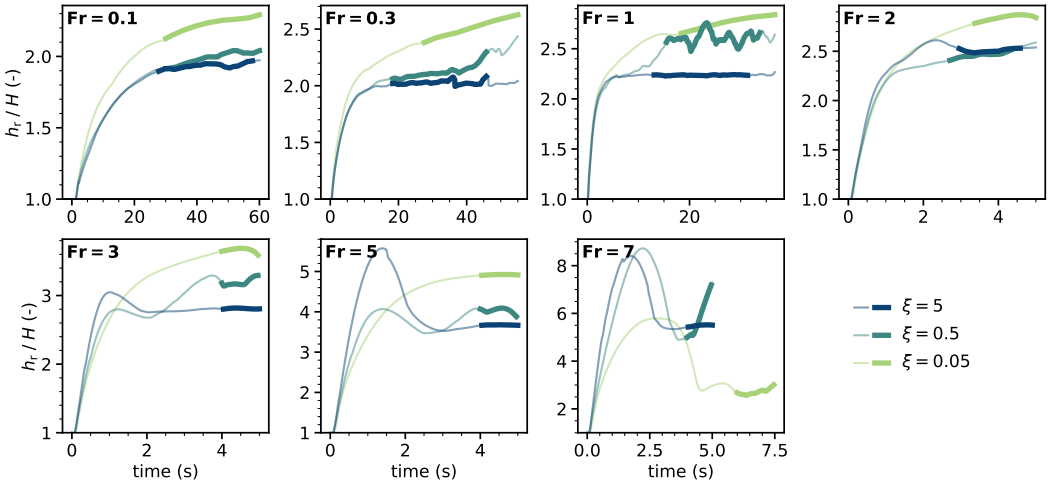


(a) Run-up height

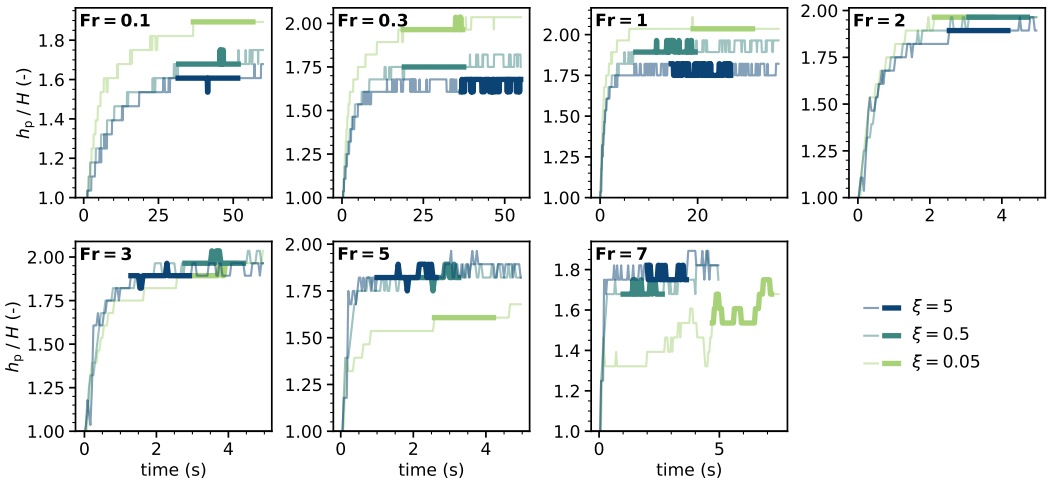


(b) Pressure height

Figure S21. Simulated rheology: $M' = 1.2$ ($M = 1.2$; $\beta = 0$)

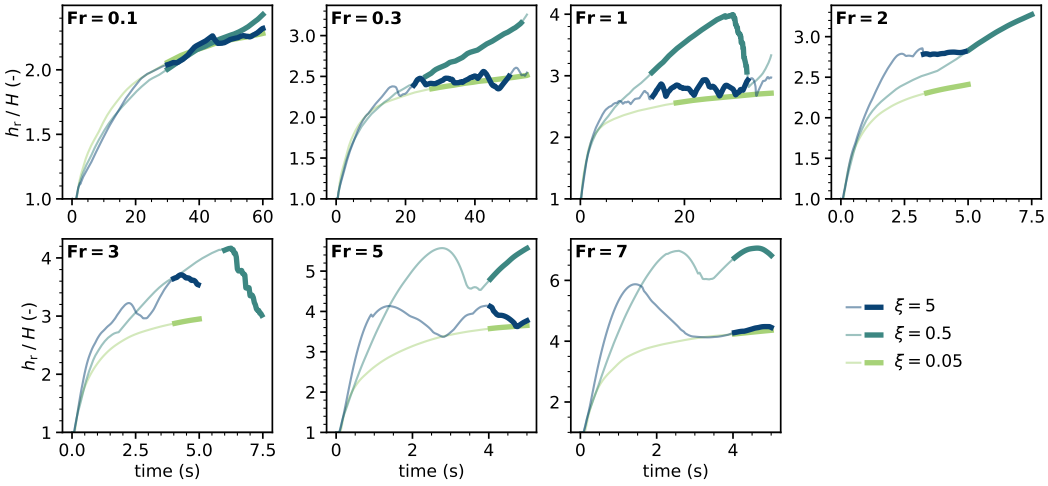


(a) Run-up height

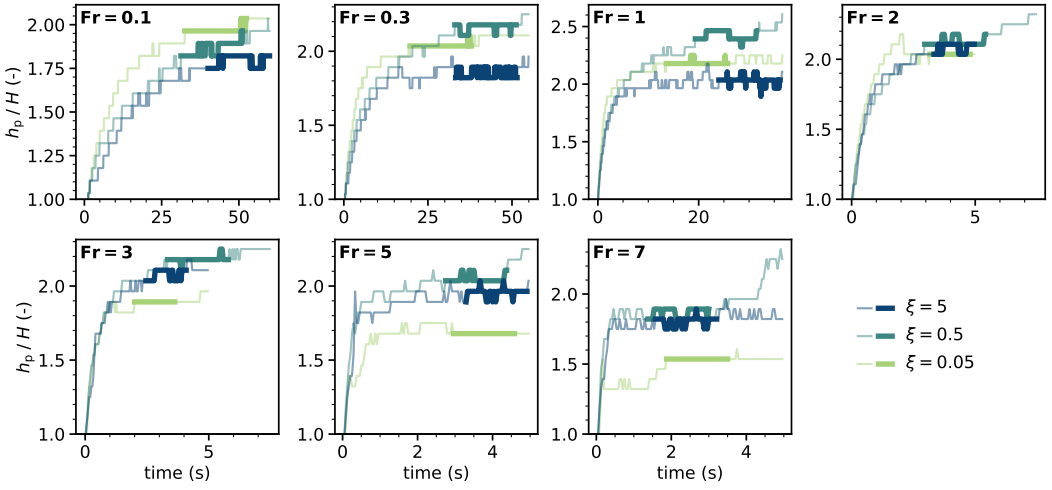


(b) Pressure height

Figure S22. Simulated rheology: $M' = 1.42$ ($M = 1.2$; $\beta = 0.15$)

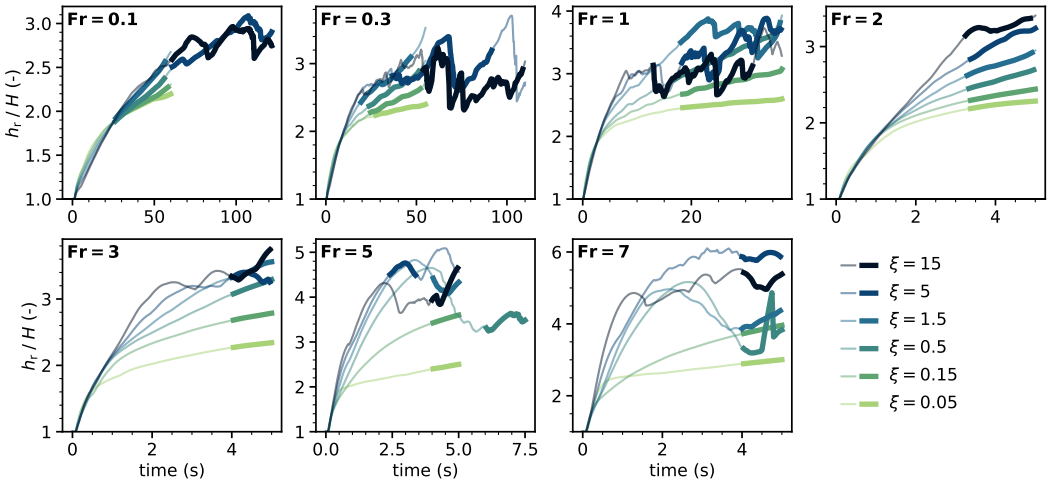


(a) Run-up height

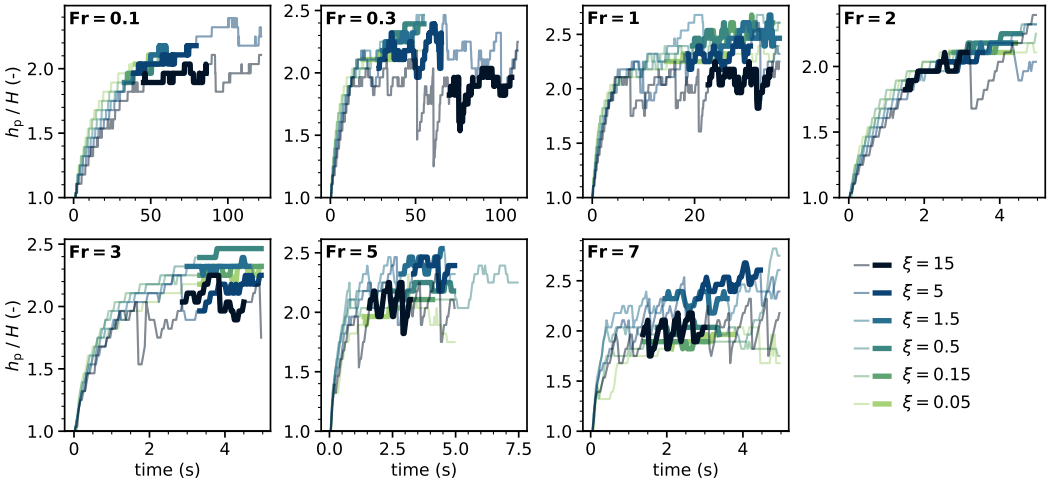


(b) Pressure height

Figure S23. Simulated rheology: $M' = 1.76$ ($M = 1.2$; $\beta = 0.3$)



(a) Run-up height



(b) Pressure height

Figure S24. Simulated rheology: $M' = 2.30$ ($M = 1.2$; $\beta = 0.45$)

S5 Peak values to steady-state values

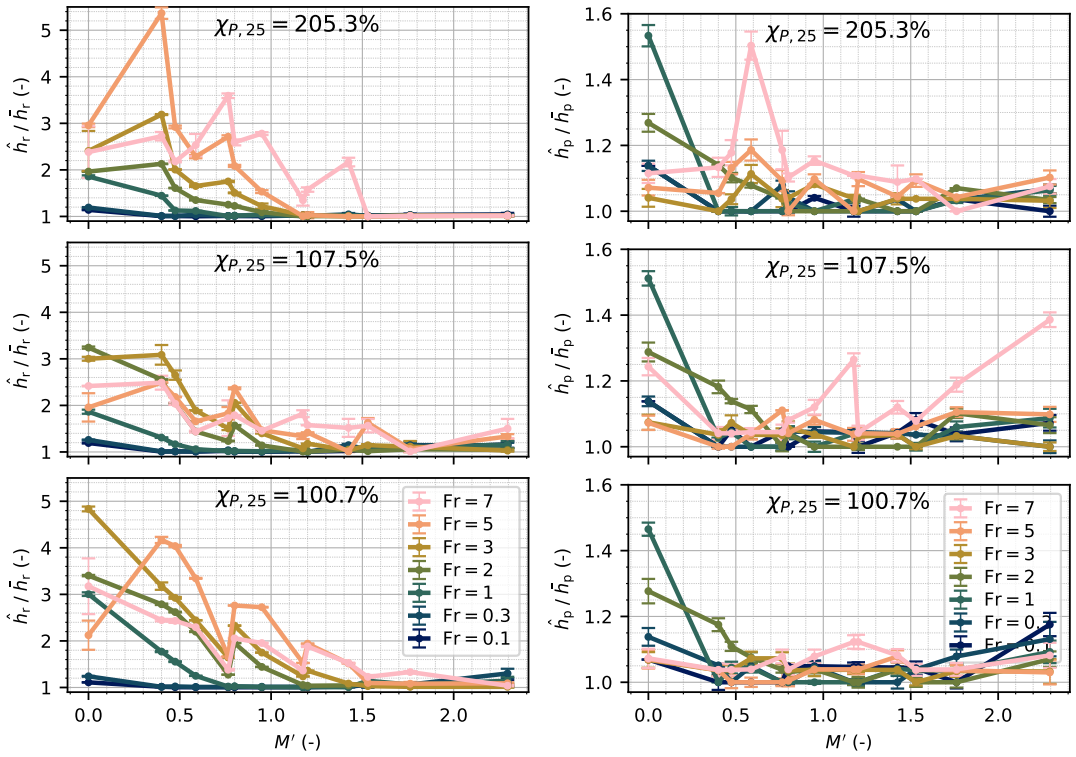
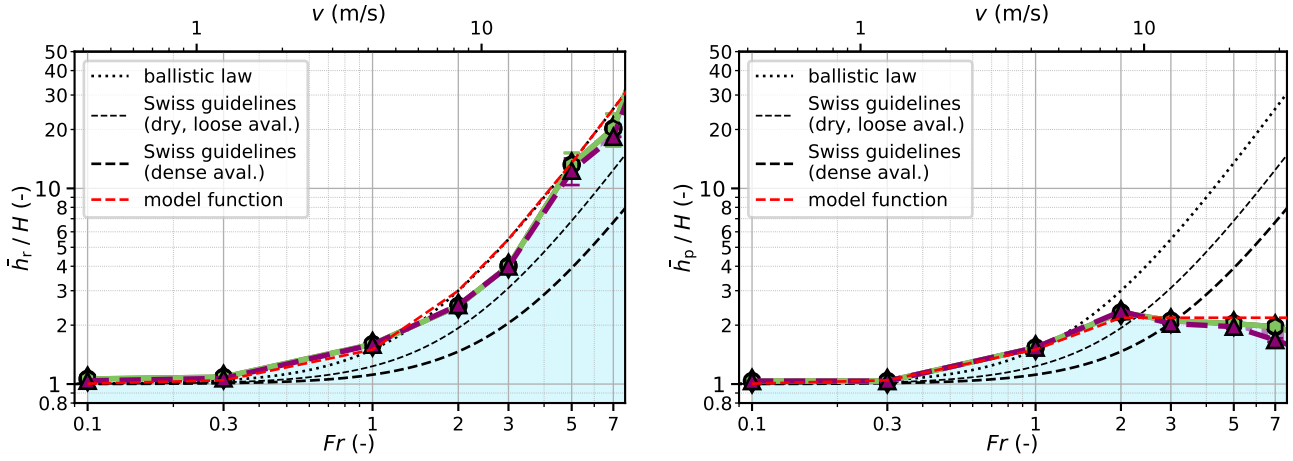


Figure S25. Peak to steady-state ratio of run-up height (left) and pressure height (right) for all studied Fr, the main compressibility configurations $\chi(p_c = 25)$ and across M'

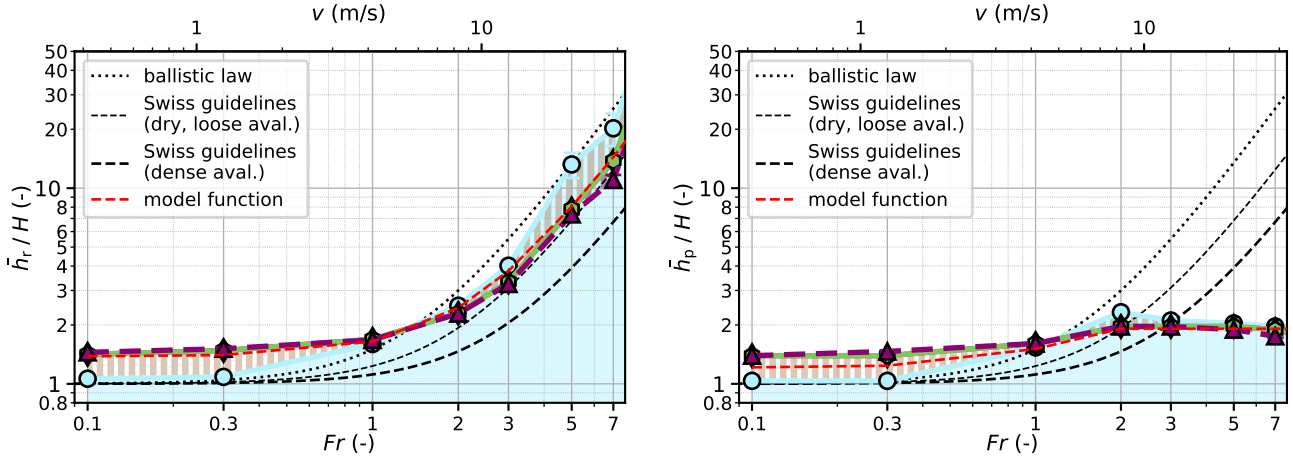
S6 Rheological decomposition



(a) Run-up height

(b) Pressure height

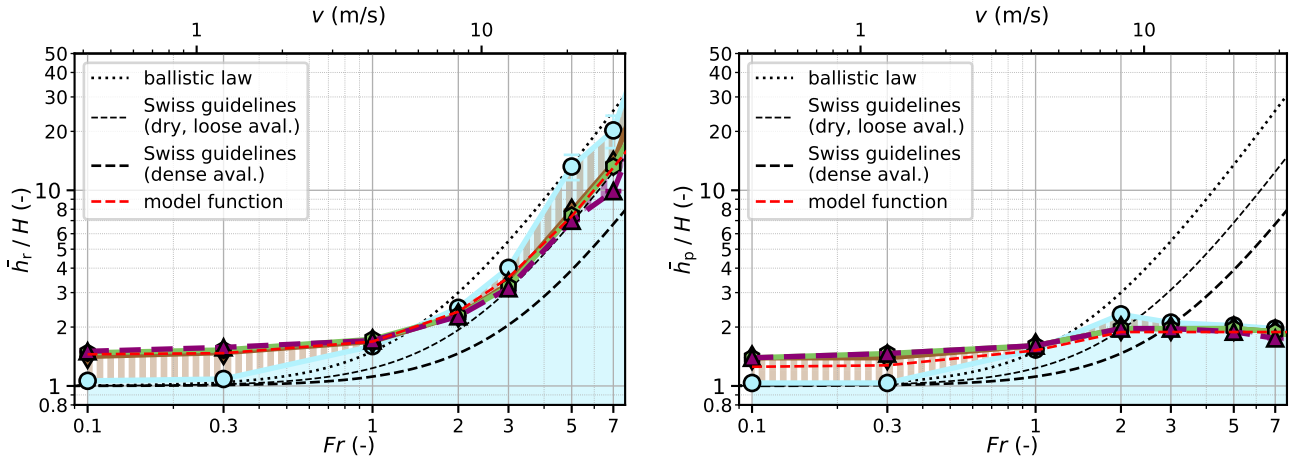
Figure S26. Rheological decomposition of $M' = 0$ ($M = 0$; $\beta = 0$)



(a) Run-up height

(b) Pressure height

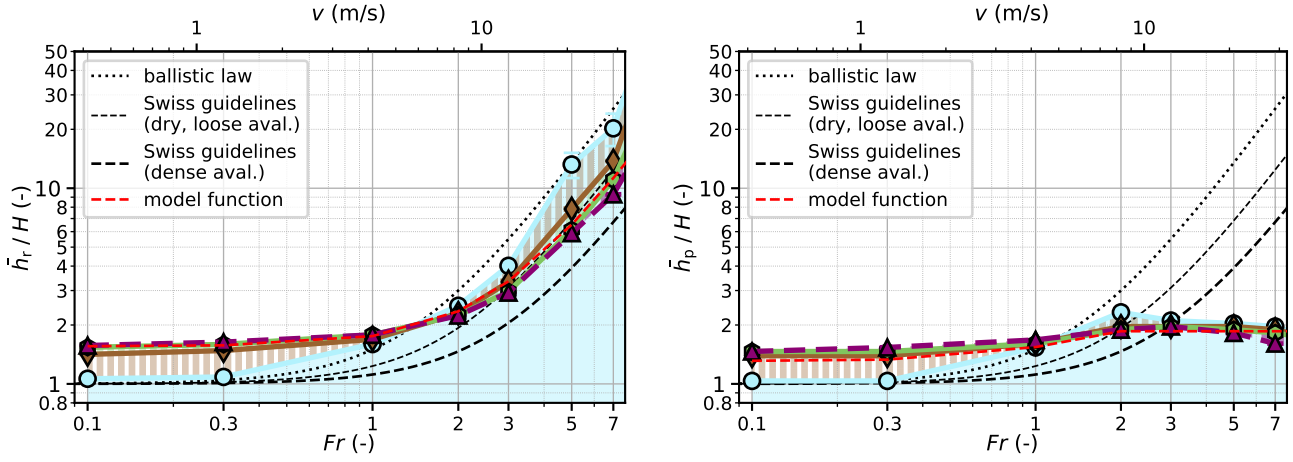
Figure S27. Rheological decomposition of $M' = 0.4$ ($M = 0.4$; $\beta = 0$)



(a) Run-up height

(b) Pressure height

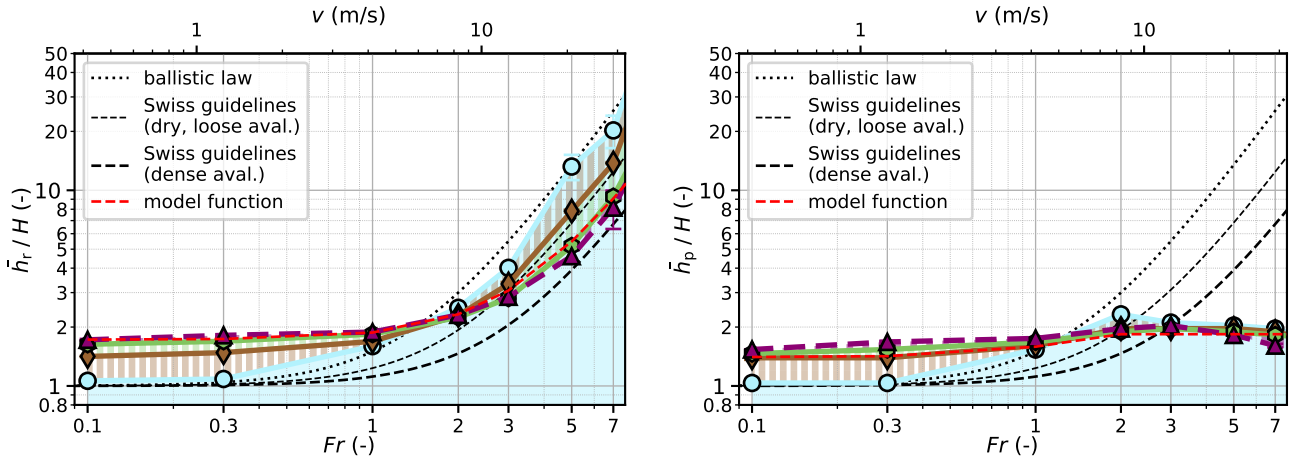
Figure S28. Rheological decomposition of $M' = 0.47$ ($M = 0.4$; $\beta = 0.15$)



(a) Run-up height

(b) Pressure height

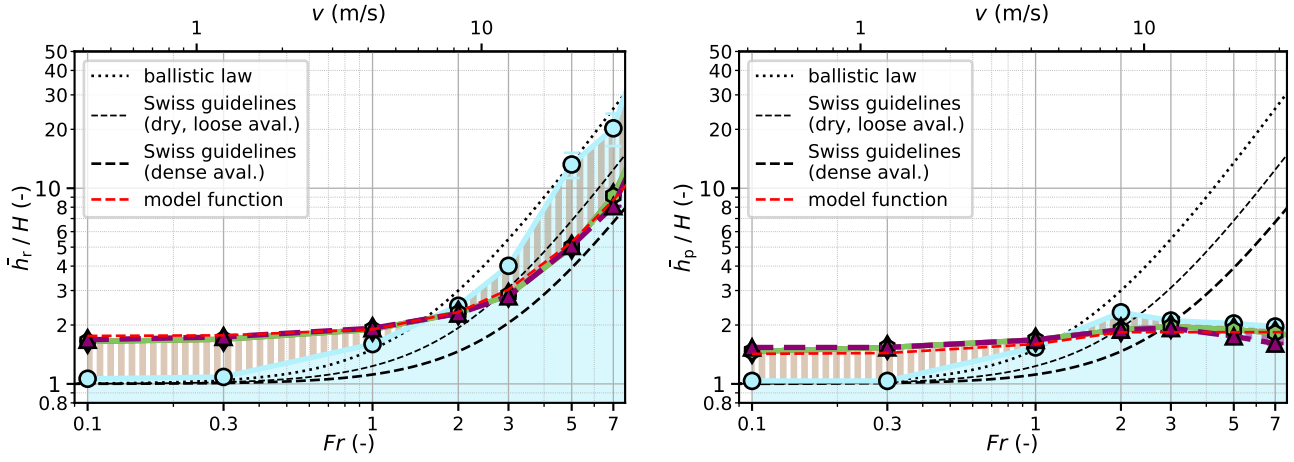
Figure S29. Rheological decomposition of $M' = 0.59$ ($M = 0.4$; $\beta = 0.3$)



(a) Run-up height

(b) Pressure height

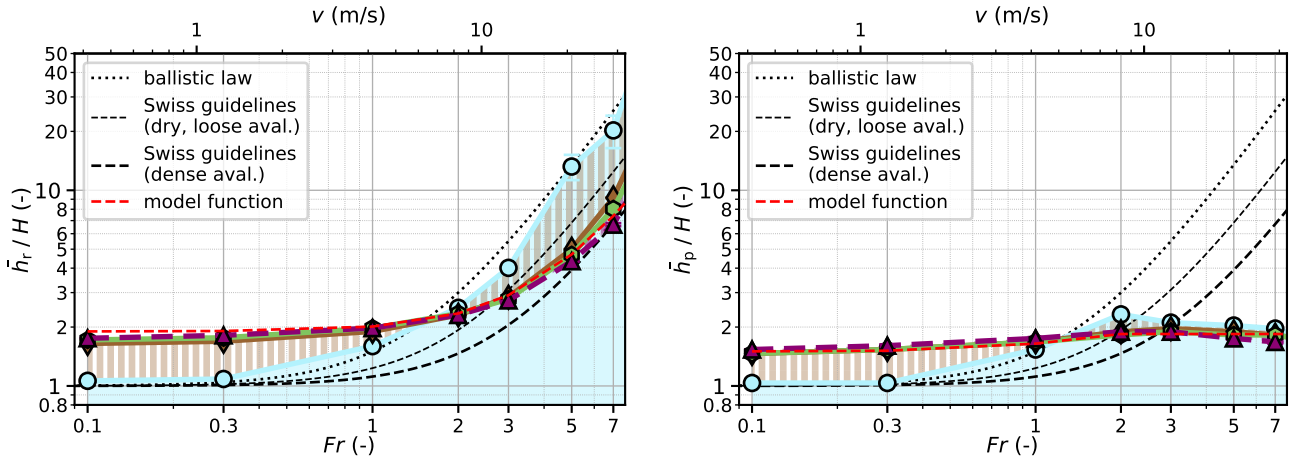
Figure S30. Rheological decomposition of $M' = 0.77$ ($M = 0.4$; $\beta = 0.45$)



(a) Run-up height

(b) Pressure height

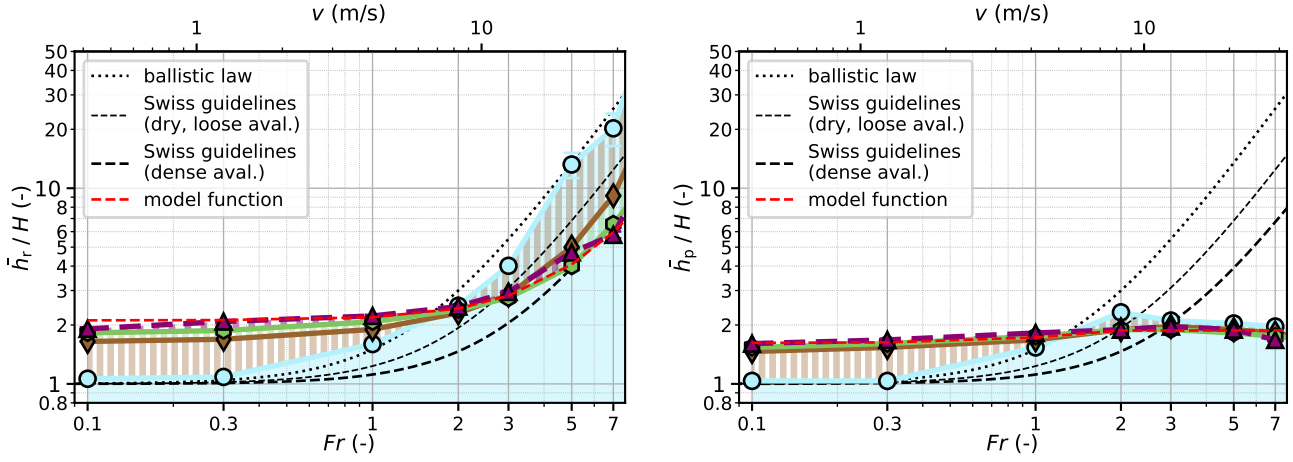
Figure S31. Rheological decomposition of $M' = 0.8$ ($M = 0.8$; $\beta = 0$)



(a) Run-up height

(b) Pressure height

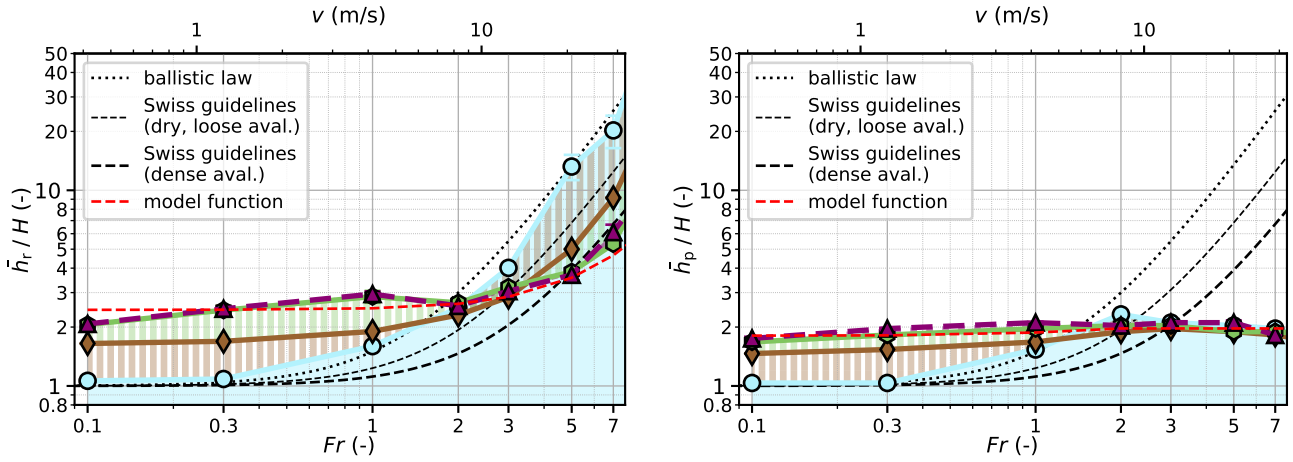
Figure S32. Rheological decomposition of $M' = 0.95$ ($M = 0.8$; $\beta = 0.15$)



(a) Run-up height

(b) Pressure height

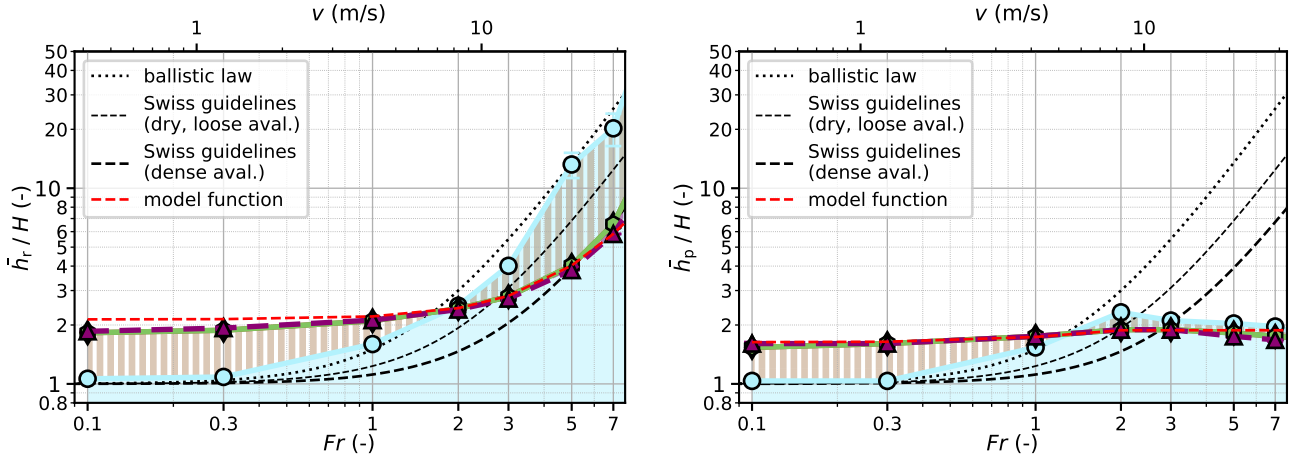
Figure S33. Rheological decomposition of $M' = 1.17$ ($M = 0.8$; $\beta = 0.3$)



(a) Run-up height

(b) Pressure height

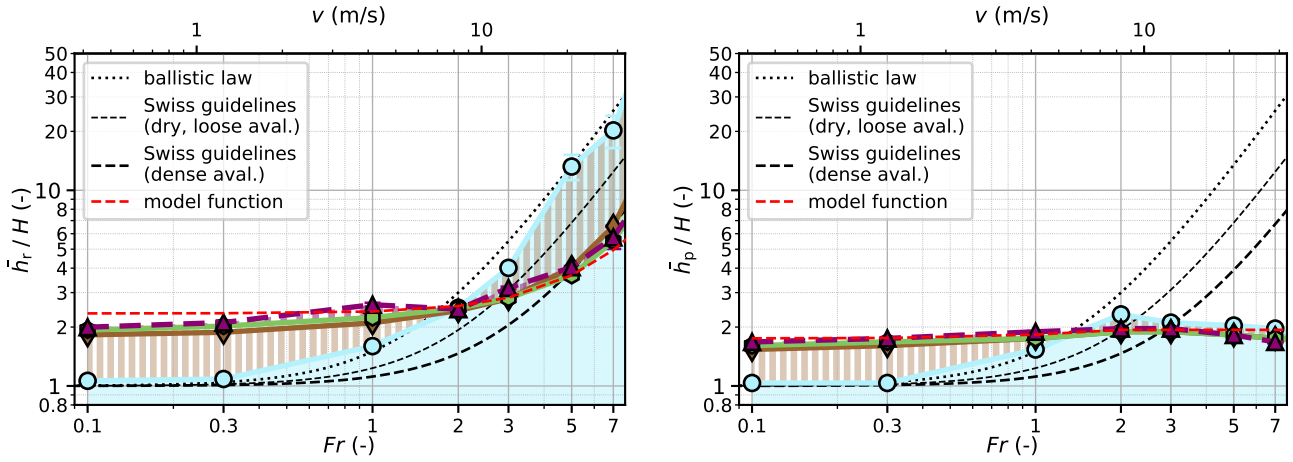
Figure S34. Rheological decomposition of $M' = 1.53$ ($M = 0.8$; $\beta = 0.45$)



(a) Run-up height

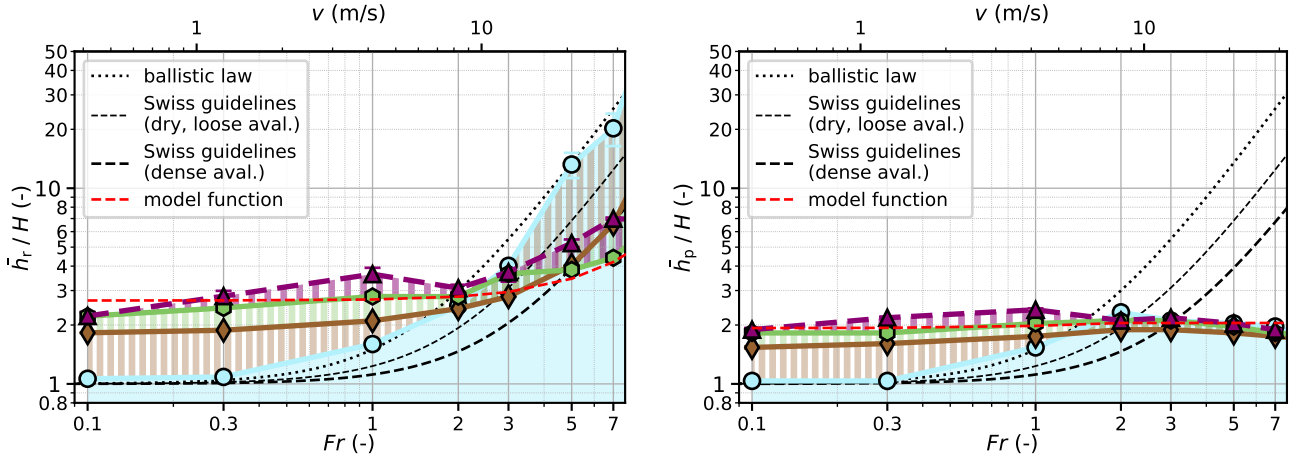
(b) Pressure height

Figure S35. Rheological decomposition of $M' = 1.2$ ($M = 1.2$; $\beta = 0$)



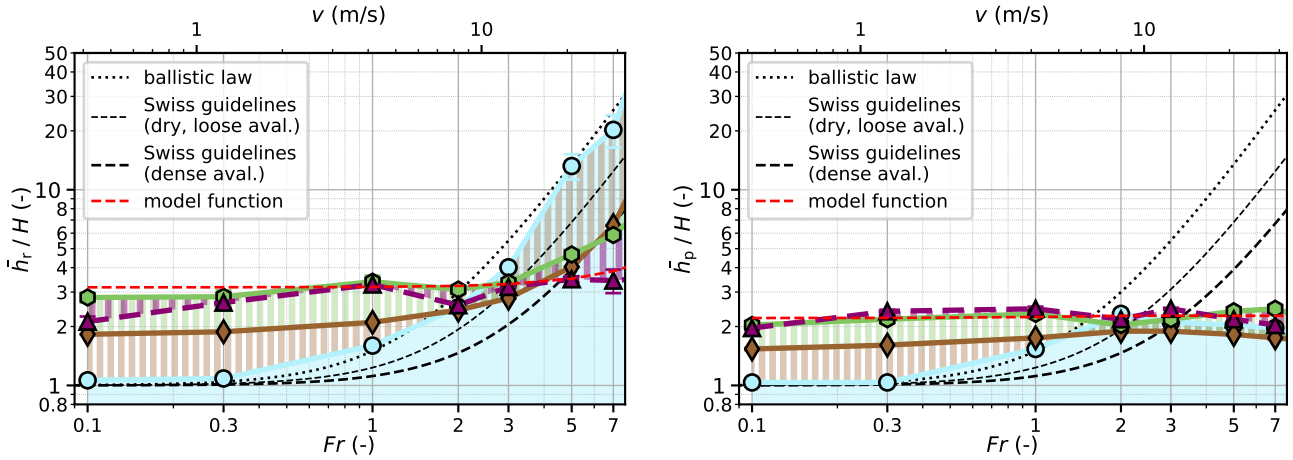
(a) Run-up height (b) Pressure height

Figure S36. Rheological decomposition of $M' = 1.42$ ($M = 1.2$; $\beta = 0.15$)



(a) Run-up height (b) Pressure height

Figure S37. Rheological decomposition of $M' = 1.76$ ($M = 1.2$; $\beta = 0.3$)

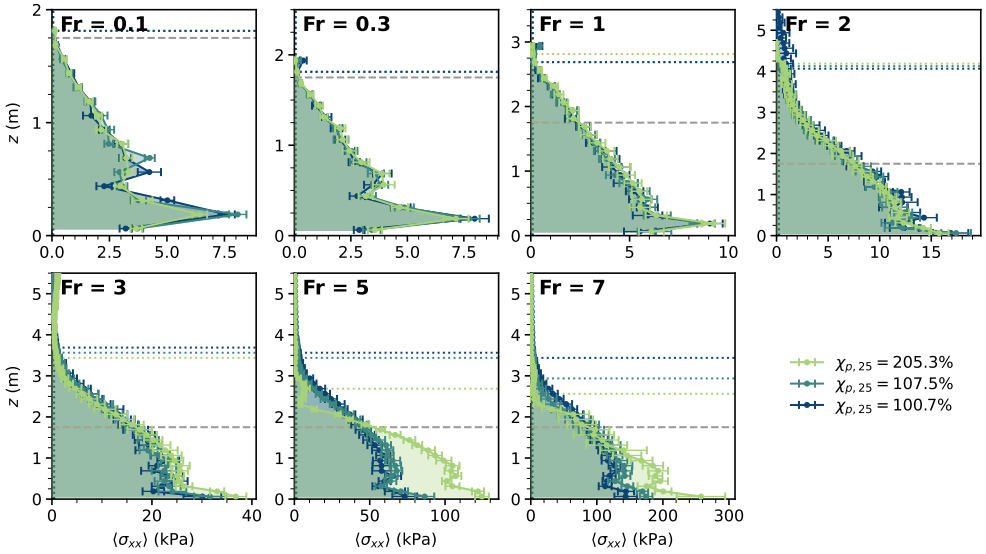


(a) Run-up height

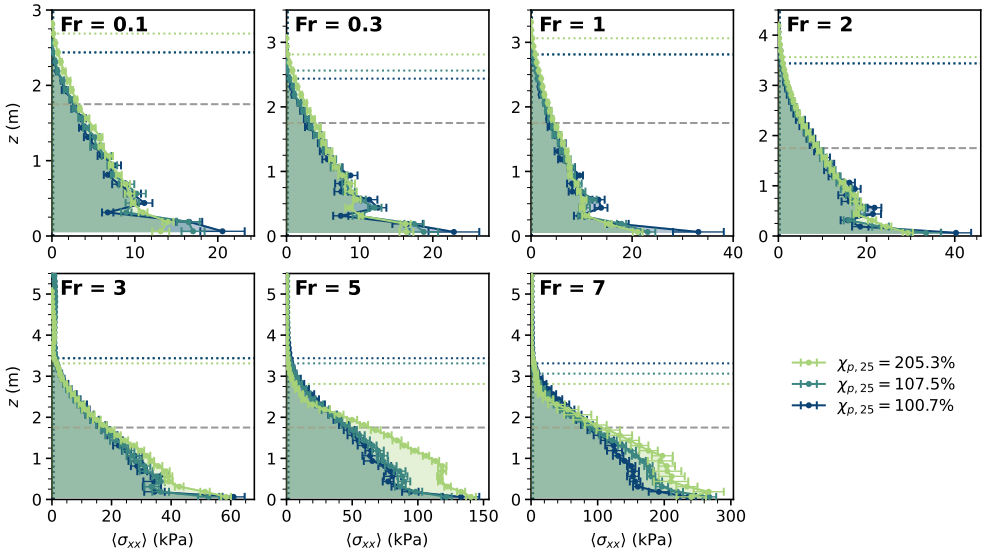
(b) Pressure height

Figure S38. Rheological decomposition of $M' = 2.30$ ($M = 1.2$; $\beta = 0.45$)

S7 Impact pressure profiles

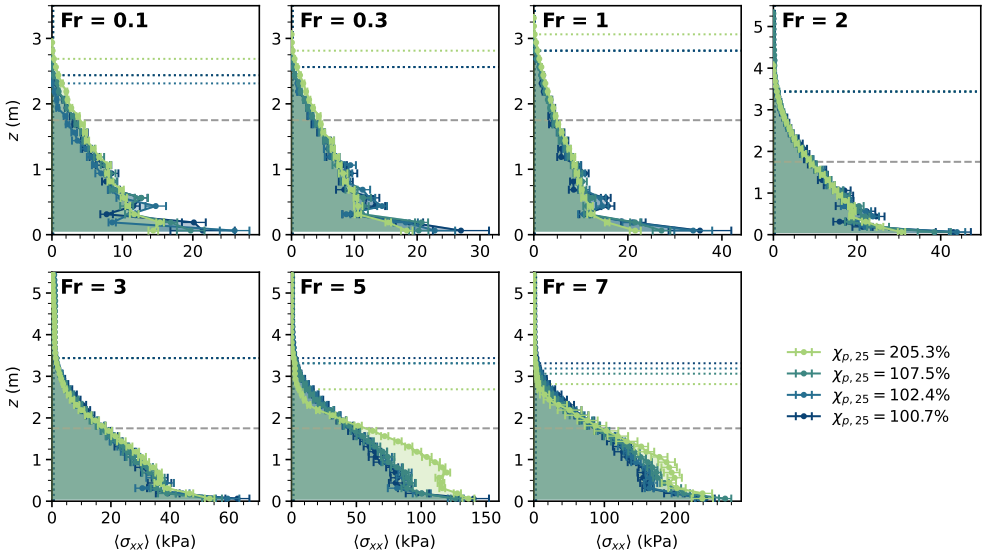


(a) $M' = 0$ ($M = 0$; $\beta = 0$)

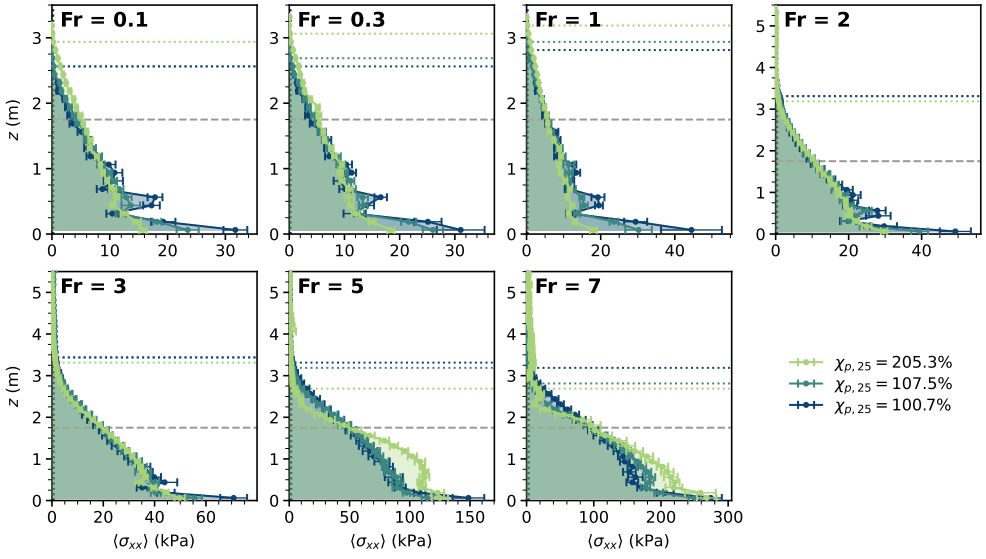


(b) $M' = 0.4$ ($M = 0.4$; $\beta = 0$)

Figure S39. Impact pressure profiles

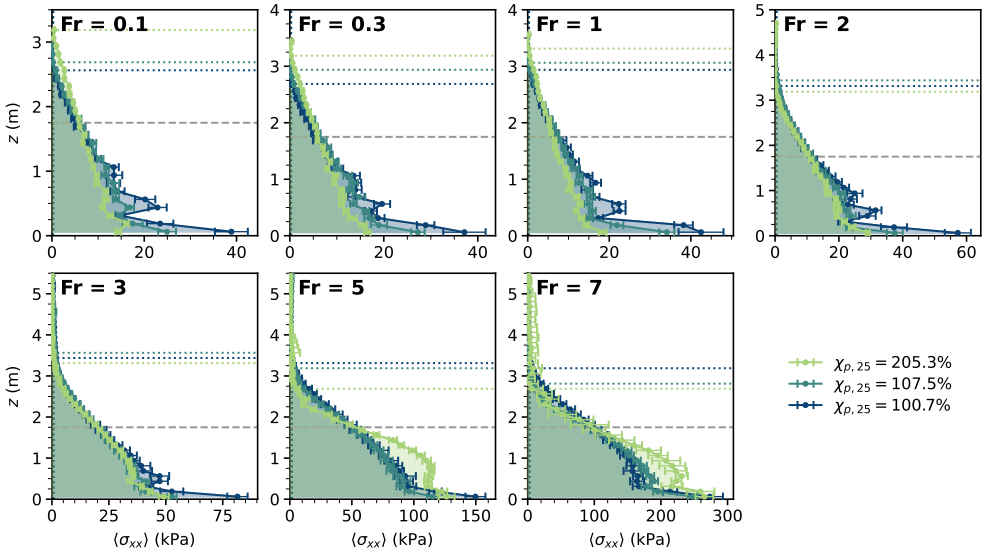


(a) $M' = 0.47$ ($M = 0.4$; $\beta = 0.15$)

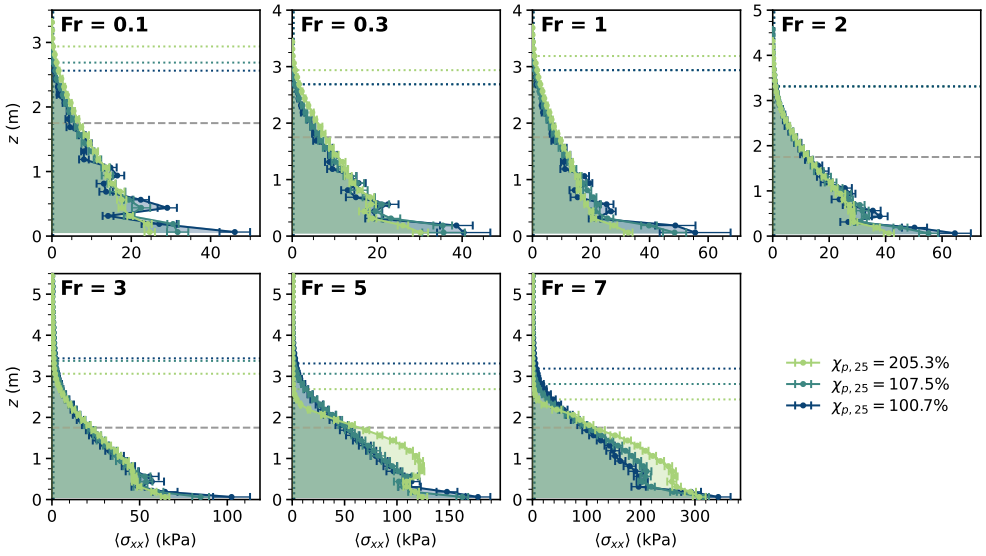


(b) $M' = 0.59$ ($M = 0.4$; $\beta = 0.3$)

Figure S40. Impact pressure profiles

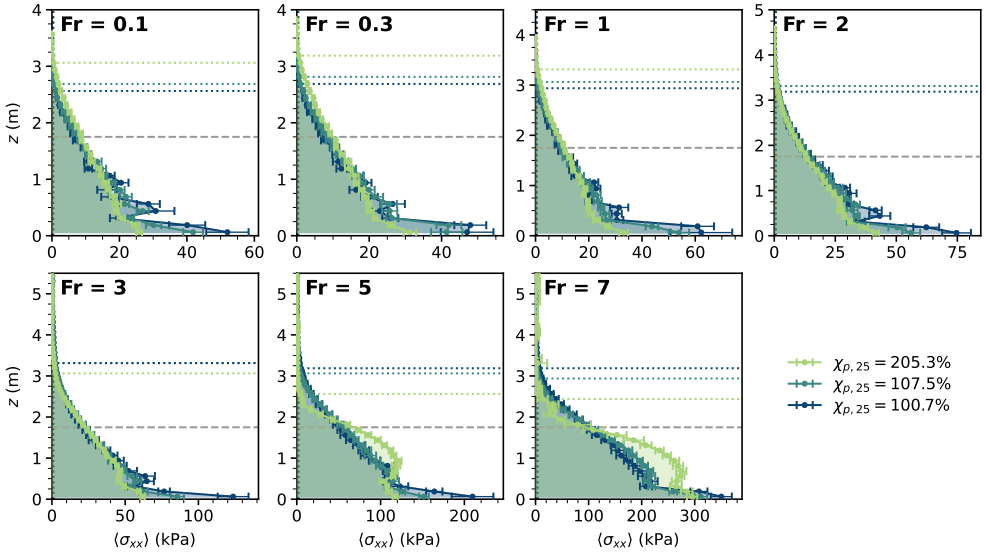


(a) $M' = 0.77$ ($M = 0.4$; $\beta = 0.45$)

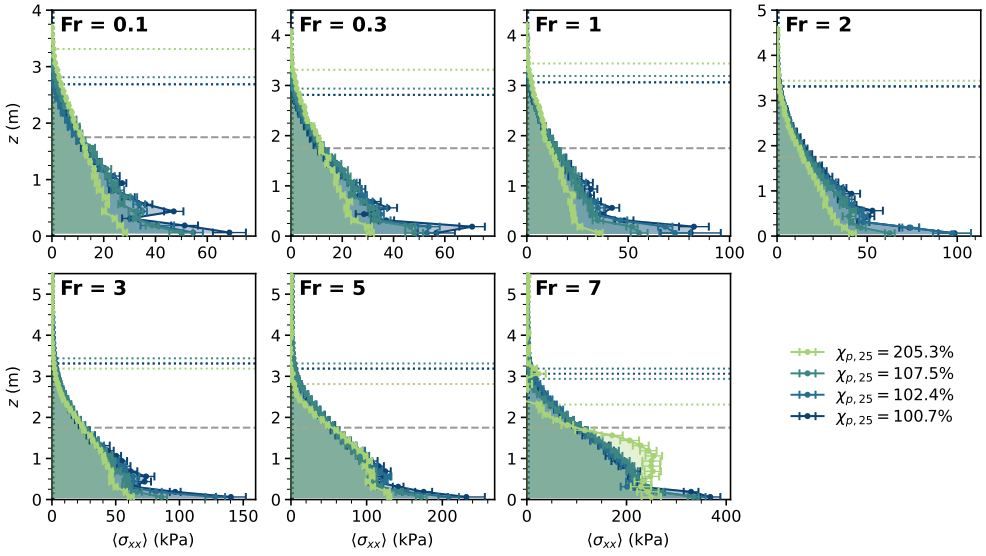


(b) $M' = 0.8$ ($M = 0.8$; $\beta = 0$)

Figure S41. Impact pressure profiles

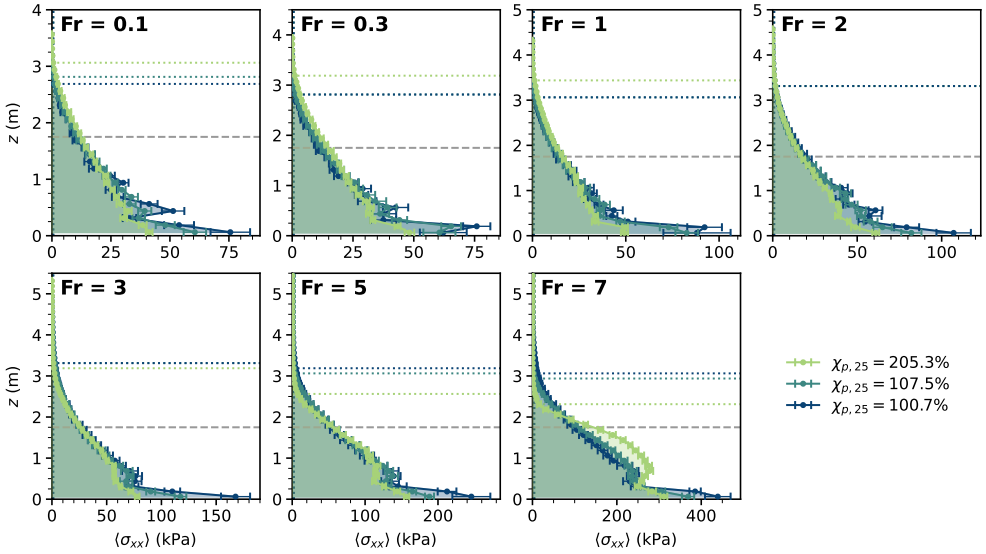


(a) $M' = 0.95$ ($M = 0.8$; $\beta = 0.15$)

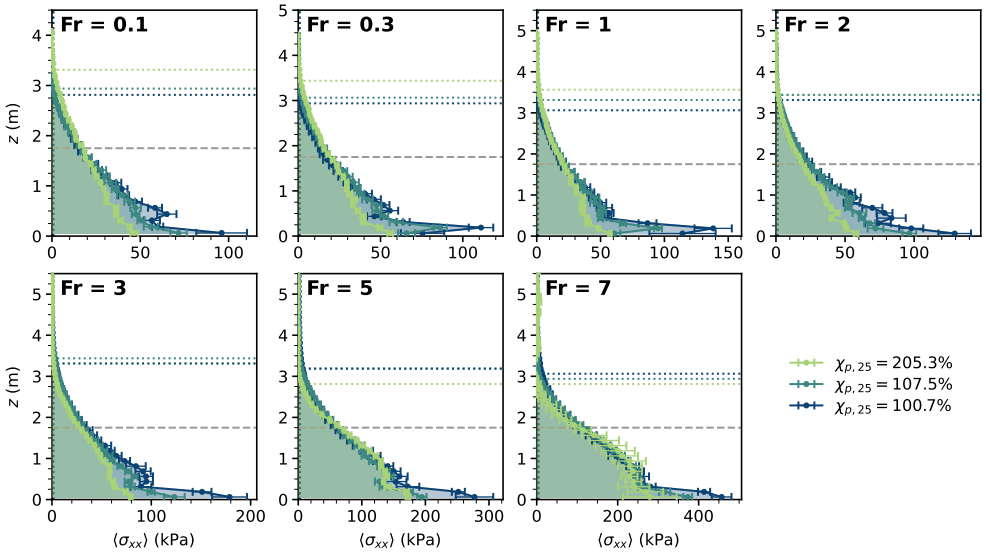


(b) $M' = 1.17$ ($M = 0.8$; $\beta = 0.3$)

Figure S42. Impact pressure profiles

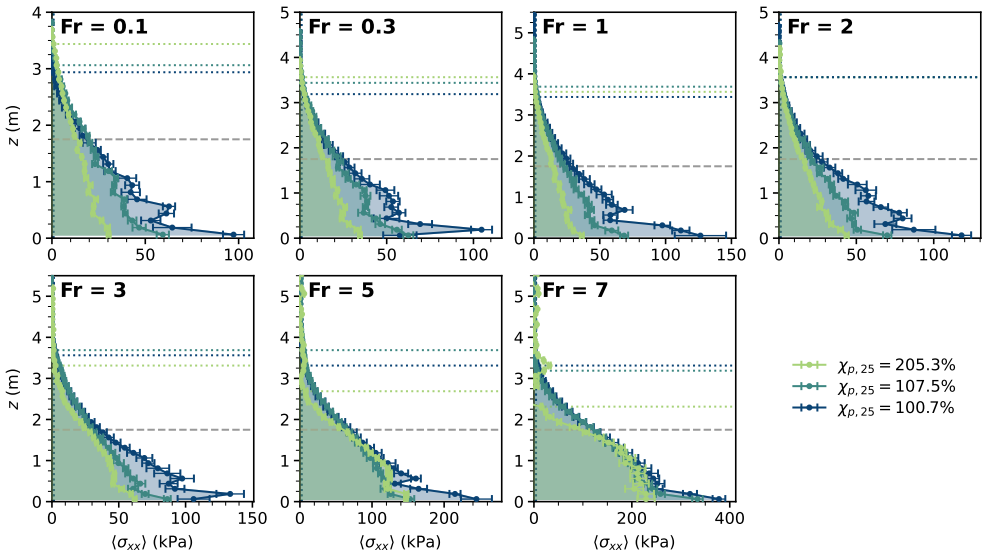


(a) $M' = 1.2$ ($M = 1.2$; $\beta = 0$)

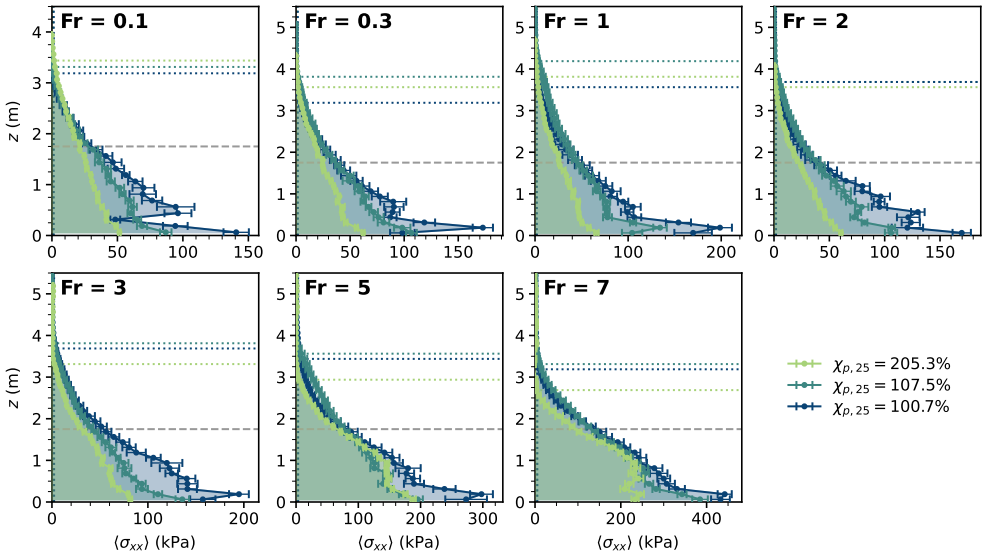


(b) $M' = 1.42$ ($M = 1.2$; $\beta = 0.15$)

Figure S43. Impact pressure profiles

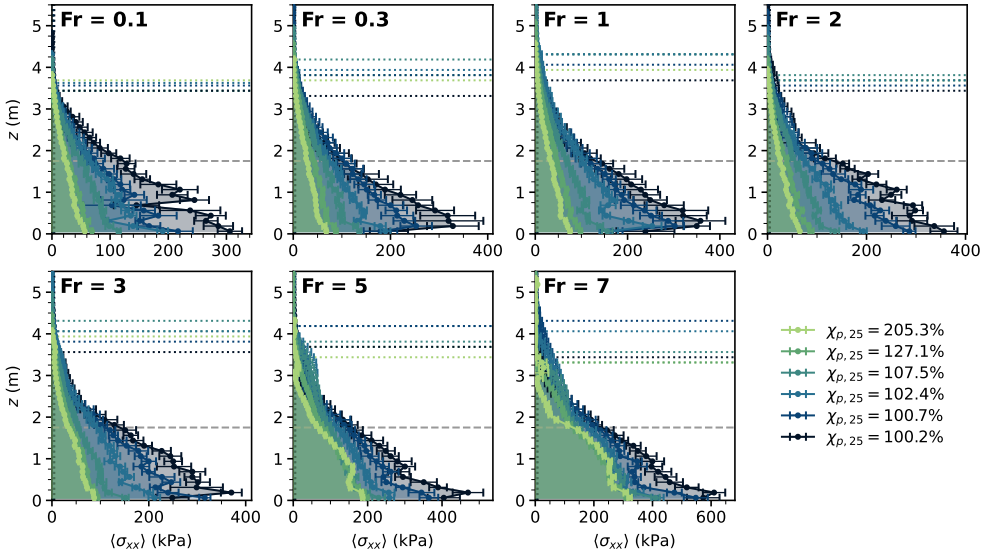


(a) $M' = 1.53$ ($M = 0.8$; $\beta = 0.45$)



(b) $M' = 1.76$ ($M = 1.2$; $\beta = 0.3$)

Figure S44. Impact pressure profiles



(a) $M' = 2.30$ ($M = 1.2$; $\beta = 0.45$)

Figure S45. Impact pressure profiles

S8 Semi-empirical modeling

S8.1 Performance metrics

Let $\{y_i\}_{i=1}^n$ denote the simulated values and $\{f_i\}_{i=1}^n$ the corresponding predictions from the semi-empirical equations, with $\bar{y} = \frac{1}{n}\sum_{i=1}^n y_i$ and $\overline{\log y} = \frac{1}{n}\sum_{i=1}^n \log y_i$. All logarithms are natural. We assume $y_i, f_i > 0$ throughout.

The following metrics assess goodness of fit in both linear and logarithmic space, capturing overall accuracy, systematic bias, and the fraction of predictions falling within specified relative tolerances. The run-up height equation is fitted and evaluated in log-space; the pressure height equation in linear space.

- Coefficient of Determination in linear space (R^2):

  $$R^2 = 1 - \frac{\sum_{i=1}^n (y_i - f_i)^2}{\sum_{i=1}^n (y_i - \bar{y})^2}.$$

  Fraction of variance in the simulated values explained by the predictions. Used to evaluate the pressure height equation.

- Coefficient of Determination in log–log space ($R^2_{\log}$):

  $$R^2_{\log} = 1 - \frac{\sum_{i=1}^n (\log y_i - \log f_i)^2}{\sum_{i=1}^n (\log y_i - \overline{\log y})^2}.$$

  Analogous to R^2, applied to log-transformed values. Used to evaluate the run-up height equation.

- Mean Normalized Root Mean Square Error (NRMSE):

  $$\mathrm{NRMSE}_{\mathrm{mean}} = \frac{1}{\bar{y}} \sqrt{\frac{1}{n}\sum_{i=1}^n (y_i - f_i)^2}.$$

  RMSE expressed as a fraction of the sample mean, giving a scale-independent measure of linear-space error. Used to evaluate the pressure height equation.

- Root Mean Square Logarithmic Error (RMSLE):

  $$\mathrm{RMSLE} = \sqrt{\frac{1}{n}\sum_{i=1}^n (\log y_i - \log f_i)^2}.$$

  RMS error in log-space, equivalent to the RMS of the log-ratios $\log(y_i/f_i)$. Approximates a typical relative error when errors are small. Used to evaluate the run-up height equation.

- Multiplicative Bias Factor:

  $$\mathrm{Bias}_{\times} = \exp\left(\frac{1}{n}\sum_{i=1}^n \log\frac{y_i}{f_i}\right).$$

  Geometric mean of the ratio y_i/f_i. Values above unity indicate systematic under-prediction; values below unity indicate over-prediction.

- Agreement Fractions:

  $$\mathrm{Frac}_p = \frac{1}{n}\sum_{i=1}^n \mathbf{1}\left(\frac{|y_i - f_i|}{y_i} \le p\right), \quad p \in \{0.10, 0.25\}.$$

  Proportion of predictions within a relative tolerance p of the simulated value.

S8.2 Run-up height

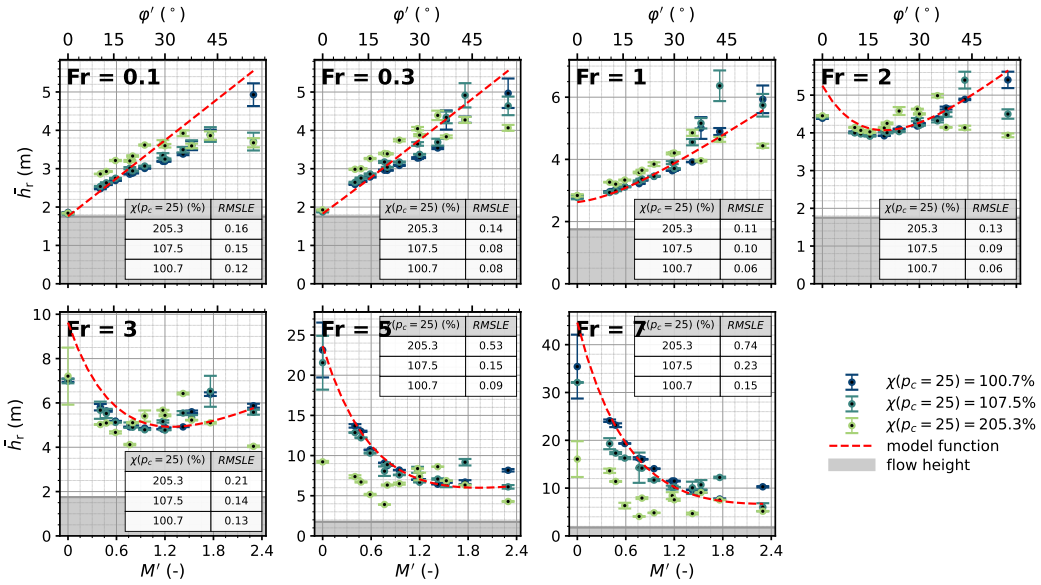


Figure S46. Run-up height over effective internal friction for three different compressibilities

Table S1. Regression coefficients and associated statistics of the run-up height equation. A bias of 0.981 translates to an over-prediction of ≈1.9%

Parameter	Value	Rel. Std. Error	t-Statistic	p-Value
$\boldsymbol{k_r}$ (-)	0.9468	0.0457	21.888	0.0
$\boldsymbol{\kappa_r}$ (-)	1.5745	0.0188	53.300	0.0

Global metrics	
$R^2_{\log}$	0.939
RMSLE	0.130
$\text{Bias}_\times$	0.981
Frac_{10}	66.3%
Frac_{25}	92.9%

Figure S47 shows how prediction accuracy varies with Fr, M', and $\chi(p_c = 25)$. The equation performs best for low to moderate plastic compressibility. For $\chi(p_c = 25) = 100.7\%$, RMSLE remains mostly below $10\,\%$ for $\text{Fr} < 3$, rising to $10\,\%$ to $15\,\%$ for $3 \leq \text{Fr} \leq 7$. For $\chi(p_c = 25) = 107.5\%$, errors are slightly larger: $7\,\%$ to $15\,\%$ for $\text{Fr} < 3$ and $14\,\%$ to $23\,\%$ for $3 \leq \text{Fr} \leq 7$. For the highly compressible case ($\chi(p_c = 25) = 205.3\%$), which lies outside the fitting range, the equation is only reliable for $\text{Fr} < 3$, where RMSLE stays below $20\,\%$. Across all compressibilities, accuracy is best for intermediate effective internal friction, $M' = 0.4$ to 1.5, where RMSLE remains at or below $10\,\%$.

S8.3 Pressure height

Figure S49 shows how prediction accuracy varies with Fr, M', and $\chi(p_c = 25)$. As for the run-up equation, accuracy is best for low to moderate plastic compressibility. For $\chi(p_c = 25) = 100.7\%$, NRMSE remains between $4\,\%$ to $8\,\%$ across the full Fr range. For $\chi(p_c = 25) = 107.5\%$, errors are slightly larger, reaching up to $14\,\%$ at high Fr. For the highly compressible case

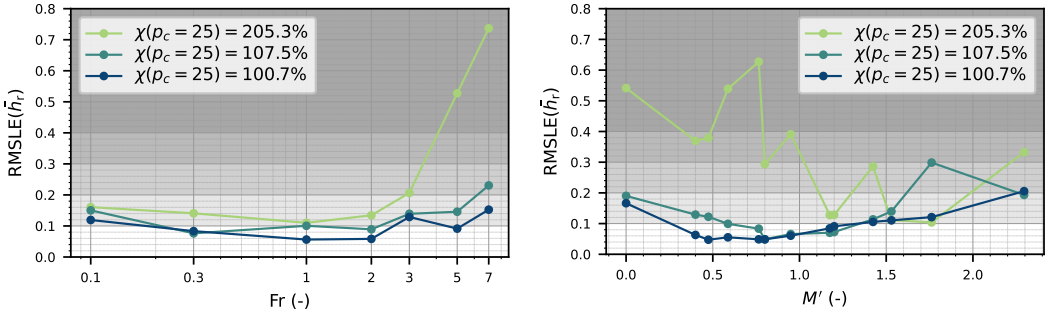


Figure S47. Left panel: RMSLE over the M' range, plotted over Fr. Right panel: RMSLE over the Fr range, plotted over M'

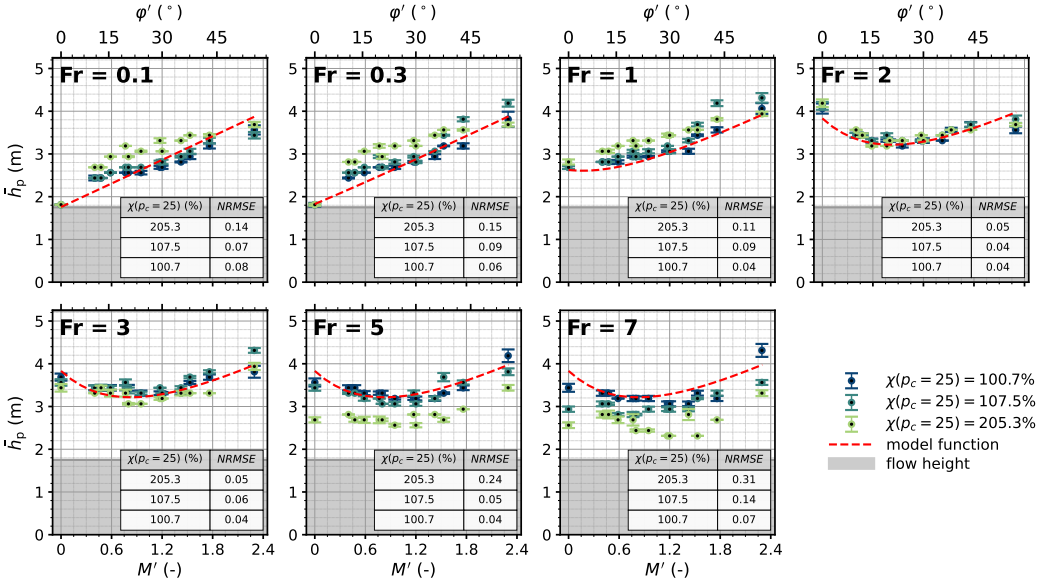


Figure S48. Pressure height over effective internal friction for three different compressibilities

Table S2. Regression coefficients and associated statistics of the pressure height equation. A bias of 1.011 translates to an under-prediction of ≈1.1%

Parameter	Value	Rel. Std. Error	t-Statistic	p-Value
$\boldsymbol{k_p}$ (-)	0.5277	0.0186	53.893	0.0
$\mathbf{Fr_{sat}}$ (-)	1.5380	0.0370	27.052	0.0
$\boldsymbol{\kappa_p}$ (-)	1.3072	0.0924	10.819	0.0

Global metrics	
R^2	0.752
$\mathrm{NRMSE_{mean}}$	0.066
$\mathrm{Bias_{\times}}$	1.011
$\mathrm{Frac_{10}}$	85.2%
$\mathrm{Frac_{25}}$	100.0%

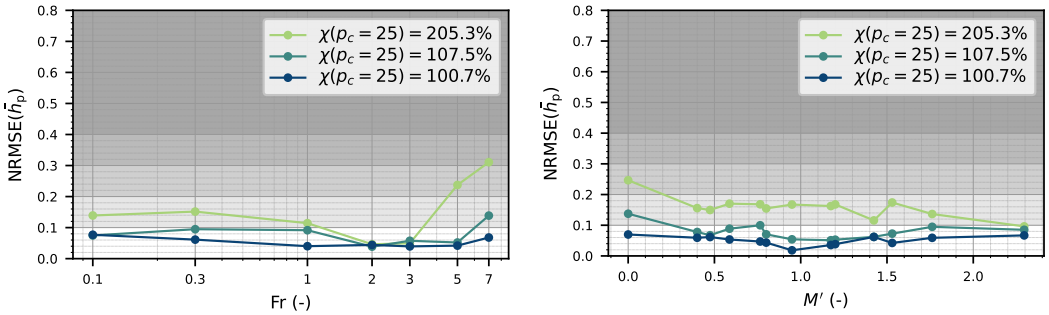


Figure S49. Left panel: NRMSE over the M' range, plotted over Fr. Right panel: NRMSE over the Fr range, plotted over M'

($\chi(p_c = 25) = 205.3\%$), NRMSE exceeds $20\,\%$ for $\mathrm{Fr} > 3$ and $M' < 0.4$. Across all compressibilities, the equation performs well for $M' \geq 0.4$, where NRMSE remains below $10\,\%$.

S9 Velocity sweep of the calculation examples

In the appendix of the article, the compared design approaches give differently ranked base reactions in the two scenarios: a dry, loose avalanche at $v = 30\,\mathrm{m\,s^{-1}}$ and a dense avalanche at $v = 10\,\mathrm{m\,s^{-1}}$. Because each scenario is only a single point in the possible velocity range, we perform two velocity sweeps in which we repeat both comparisons over a velocity range. All the other parameters retain the values defined in the scenario of each example (cf. Table A1 in the body of the article).

In each sweep, we retain all flow-regime-related calculation assumptions (e.g., dissipation factor, drag coefficient, and M') and cover a range of speeds in which the flow regime considered is plausible (Rudolf-Miklau et al., 2014). For the dense avalanche scenario, we compare our results only with the predictions from the Swiss guidelines, using the unlimited run-up height with $\lambda = 3$ and $M' = 1.2$. For the dry, loose snow avalanche scenario, we compare our results with the predictions from the Swiss guidelines limited to $v/10\,\mathrm{s^{-1}}$ and with the *EC handbook*, using $\lambda = 1.5$, $M' = 0.65$ and $C_\mathrm{D} = 1$ above the flow depth for the *EC handbook* curve. Both figures use logarithmic y-axes, on which a power law of the velocity appears as a straight line of slope equal to its exponent.

S9.1 Original scenario: dry, loose impact

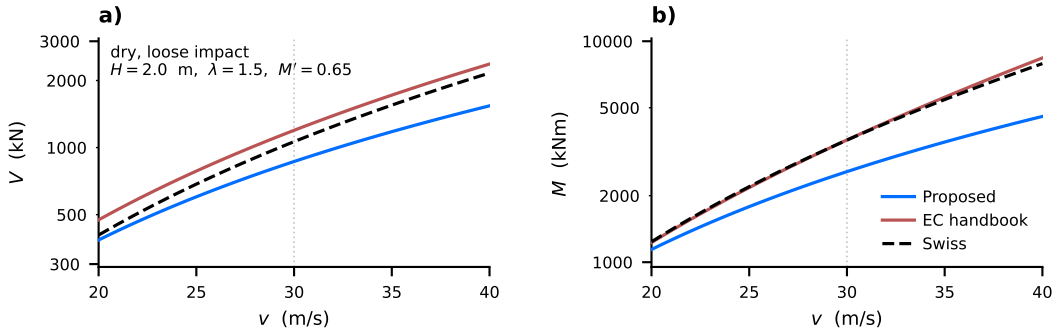


Figure S50. Base shear (a) and base moment (b) against the front velocity for the dry, loose scenario, $v = 20\,\mathrm{m\,s^{-1}}$ to $40\,\mathrm{m\,s^{-1}}$, comparing the proposed approach with the Swiss recommendations limited to $v/10\,\mathrm{s^{-1}}$ and with the *EC handbook* at $\lambda = 1.5$ and $M' = 0.65$. The dotted vertical line marks $v = 30\,\mathrm{m\,s^{-1}}$, the velocity of the example scenario shown in the appendix of the main manuscript. Note the logarithmic y-axes.

In the dry, loose regime (cf. Fig. S50), our approach gives the smallest forces over the whole range, and the margin widens with velocity. Relative to the Swiss guidelines, the base shear falls from $-5\,\%$ at $20\,\mathrm{m\,s^{-1}}$ to $-29\,\%$ at $40\,\mathrm{m\,s^{-1}}$, and the base moment from $-8\,\%$ to $-42\,\%$; relative to the *EC handbook*, from $-19\,\%$ to $-35\,\%$ in V and from $-7\,\%$ to $-46\,\%$ in M. The reason is again the saturation of the pressure height, while the loaded height of the other two approaches grows with the velocity. The base moments of the two reference approaches nearly coincide over the entire range. They are, however, composed differently: the Swiss recommendations concentrate the load in a single triangle above the flow depth, whereas the *EC handbook* distributes it over the snow cover, the fluidized layer and the powder cloud, whose large lever arm compensates for its small resultant.

S9.2 Modified scenario: dense impact

In the dense regime (cf. Fig. S51), the inertia-driven part of the pressure height is saturated over the entire velocity range, so the pressure height itself does not grow with v^2; only the magnitude of the dynamic pressure does. In the Swiss recommendations, by contrast, both the run-up height and the dynamic pressure grow with v^2, so their $V(v)$ and $M(v)$ curves are steeper. The two sets of curves cross at $v \approx 13\,\mathrm{m\,s^{-1}}$ in both quantities. Below this velocity, our approach is the more conservative one, by $15\,\%$ in V and $25\,\%$ in M at $10\,\mathrm{m\,s^{-1}}$, because it accounts for a gravity-driven contribution that persists at low velocity; above it, our approach gives the smaller actions, by $27\,\%$ in V and $40\,\%$ in M at $20\,\mathrm{m\,s^{-1}}$.

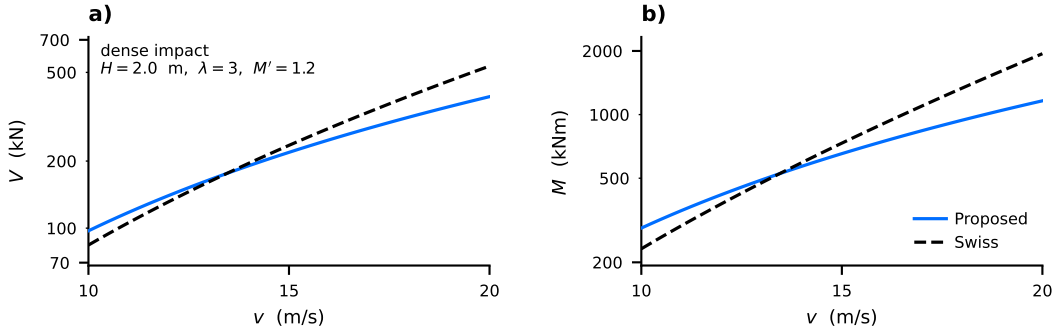


Figure S51. Base shear (a) and base moment (b) against the front velocity for the dense scenario, $v = 10\,\mathrm{m\,s^{-1}}$ to $20\,\mathrm{m\,s^{-1}}$, comparing the proposed approach at $M' = 1.2$ with the Swiss recommendations at $\lambda = 3$. Note the logarithmic y-axes.

References

Kohler, M. J., Gaume, J., Ancey, C., and Sovilla, B.: 3D Numerical Modeling of Compressible and Cohesive Granular Flow Impact on Narrow Obstacles, Computational Particle Mechanics, 13, 79–96, https://doi.org/10.1016/j.cpms.2025.11.005, 2026.

Rudolf-Miklau, F., Sauermoser, S., and Mears, A. I., eds.: The Technical Avalanche Protection Handbook, Wiley, 1 edn., https://doi.org/10.1002/9783433603840, 2014.